Mid-infrared spectroscopy of sulfidation reaction products and implications for Sulfur on Mercury

C. J. Renggli[1], Stojic A.N. [2], A. Morlok[2], J. Berndt[1], I. Weber[2], S. Klemme[1], H. Hiesinger[2]

[1] Institut für Mineralogie, Universität Münster, Münster, 48149, Deutschland

[2] Institut für Planetologie, Universität Münster, Münster, 48149, Deutschland

Corresponding author: Christian Renggli (renggli@uni-muenster.de)

ORCID: Renggli 0000-0001-8913-4176

Stojic 0000-0002-9037-3243

Morlok 0000-0001-6290-2147

Berndt 0000-0002-6766-3066

Weber 0000-0001-7598-3951

Klemme 0000-0001-7859-9779

Hiesinger 0000-0001-7688-1965

Key points

- S-enrichment on the surface of Mercury by sulfidation of silicate minerals
- Mid-IR spectroscopy allows the identification of quartz as a main reaction product in mineral and glass sulfidation.
- BepiColombo's MERTIS instrument will test the sulfidation hypothesis by mapping the surface of Mercury in the mid-IR spectral range.

Abstract

We propose that the observed enrichment of sulfur at the surface of Mercury (up to 4 wt.%) is the product of silicate sulfidation reactions with a S-rich reduced volcanogenic gas phase. Here, we present new experiments on the sulfidation behavior of olivine, diopside, and anorthite. We investigate these reaction products, and those of sulfidized glasses with Mercury compositions previously reported, by mid-IR reflectance spectroscopy. We investigate both the reacted bulk materials as powders, as well as cross-sections of the reaction products by in-situ micro-IR spectroscopy. The mid-IR spectra confirm the presence of predicted reaction products including quartz. The mid-IR reflectance of sulfide reaction products, such as CaS (oldhamite) or MgS (niningerite), is insufficient to be observed in the complex run products. However, the ESA/JAXA BepiColombo mission to Mercury will be able to test our hypothesis by investigating correlated abundances of sulfides with other reaction products such as quartz.

Plain language summary

The surface of the planet Mercury is enriched in sulfur, with abundances of up to 4 wt.%. Sulfur on Mercury has previously been interpreted to occur in magmatic sulfide phases. We propose an alternative mechanism for the enrichment of S on Mercury, whereby reduced S-rich gases react with silicate minerals to form sulfides and quartz. We carried out sulfidation experiments on silicate minerals and glasses and used mid-infrared spectroscopy to characterize the products of these reactions. The upcoming ESA/JAXA BepiColombo mission to Mercury will allow us to test the sulfidation hypothesis and provide constraints on the origin of the S enrichment on the planet's surface.

Introduction

The surface of Mercury is distinctly enriched in S, with up to 4 wt. % as revealed by the NASA MErcury Surface, Space ENvironment, GEochemistry and Ranging (MESSENGER) spacecraft (McCoy et al., 2018; Larry R. Nittler et al., 2011; Larry R Nittler et al., 2018; Weider et al., 2015). The processes that resulted in the enrichment of S on the surface of Mercury remain unresolved, however,

several processes have been proposed. At extremely reducing conditions several logfO_2 units below the Iron-Wüstite buffer (IW), at IW-3 to IW-7, the solubility of S in basaltic melts is high and increases with decreasing fO_2 (Anzures, Parman, Milliken, Lanzirotti, et al., 2020; Anzures, Parman, Milliken, Namur, et al., 2020; Cartier et al., 2014; Namur et al., 2016). Assuming that melts on Mercury experience no oxidation from the highly reduced mantle source, sulfides in lavas on the surface of Mercury may be of primary magmatic origin (Anzures, Parman, Milliken, Namur, et al., 2020; Namur et al., 2016; Mikhail Y. Zolotov et al., 2013). However, if the magmas experienced even minor degrees of oxidation from the mantle source to the surface, the solubility of S would have decreased from approximately 7 wt.% at IW-7, to 3 wt.% at IW-5, and 1 wt.% at IW-3 (Namur et al., 2016), resulting in the degassing of S. Processes that could have resulted in the oxidation of ascending magmas on Mercury include assimilation of oxides into the melts (Mikhail Yu. Zolotov, 2011), decompression oxidation (e.g. Foley, 2011), or smelting processes (Iacovino et al., 2023; McCubbin et al., 2017). Previously, it was argued that such oxidation mechanisms have resulted in the formation of volcanic gases that drive explosive volcanism on Mercury (Deutsch et al., 2021; Iacovino et al., 2023; Kerber et al., 2011; L. R. Nittler et al., 2014; Weider et al., 2016), including the depletion of pyroclastic deposits in the degassed volatiles, as observed in the S depleted Nathair Facula, NE of Rachmaninov crater (Weider et al., 2016).

Sulfur species in hot volcanic gases are highly reactive with silicate minerals and glasses (King et al., 2018). At oxidizing conditions a SO_2 disproportionation reaction forms sulfate coatings on glasses (Renggli, Palm, et al., 2019; Christian J Renggli & King, 2018), whereas at reducing conditions gas species including S_2, COS, and CS_2 react with glasses and minerals to form sulfides including troilite (FeS), oldhamite (CaS), and niningerite (MgS) (C.J. Renggli et al., 2022). We have previously argued that these sulfidation reactions may be responsible for the observed enrichment of S on the surface of Mercury. For example, the sulfidation of the primary predicted silicate minerals anorthite, forsterite, and diopside (Namur & Charlier, 2017) with CS_2 gas can be written as:

$$Mg_2SiO_4 + CaMgSi_2O_6 + 2CaSi_2Al_2O_8 + 3CS_{2(g)} \rightarrow \{7SiO_2 + 2Al_2O_3\}_{glass;\,melt;\,mineral} + 3CaS + 3MgS + 6CO_{(g)} \quad \textit{Equation 1}$$

In addition to the sulfides, these reactions result in the formation of quartz and aluminosilicate phases (C.J. Renggli et al., 2022). Since quartz is not predicted to be present in most Mercury terranes, and as an accessory phase only in the low-Mg terrane and the Caloris interior plains (McCoy et al., 2018; Namur & Charlier, 2017), quartz presence on the surface of Mercury, together with sulfides such as oldhamite and niningerite, is evidence for sulfidation reactions.

Sulfidation results in a change of spectral properties due to the change in mineralogy. In this study we use the experimental run products (low-Mg, high-Mg, and high-Al glasses) from Renggli et al. (2022), and run additional sulfidation experiments at 800, 1000, and 1200 °C of olivine, diopside, and anorthite, to determine the change in the mid-infrared spectra. We investigated the reaction products using electron microscopy and micro-FTIR (Fourier Transform Infrared Spectroscopy), in the mid-IR from 2.5-16.7 µm (equivalent to 4000 to 666 cm^{-1}), to characterize their chemistry, mineralogy and spectral properties. The spectral data of the sulfide coatings will be used as a reference for the MERTIS spectrometer (Mercury Radiometer and Thermal Infrared Spectrometer) onboard the BepiColombo (ESA/JAXA) mission to Mercury (Hiesinger & Helbert, 2010). The observations from BepiColombo will allow testing of our proposed mechanism for the formation of surface sulfides on Mercury by high-temperature gas-solid reactions with reduced S-rich gas. The ID-numbers of samples reported here refer to the IRIS (Infrared and Raman for Interplanetary Spectroscopy) database hosted at the Institute for Planetology, University of Münster (http://bc-mertis-pi.uni-muenster.de/), where the data is publicly available.

Methods

Experiments

In this study we present mid-IR spectroscopic observations from silicate glass sulfidation experiments that we previously reported (Renggli et al. 2022). We refer the reader to that publication for details on the synthesis of the glasses with compositions based on observations from the NASA MESSENGER mission. The glasses include a low-Mg sample (ID 174), based on the low-Mg Northern Volcanic Plains, a high-Mg sample (ID 156), based on the similarly named high-Mg region, and a high-

Al sample (ID155) based on terrains southwest and southeast of the northern volcanic plains (Namur & Charlier, 2017; Vander Kaaden et al., 2017). The mid-IR spectral properties of these pristine glasses are described in Morlok et al. (2021).

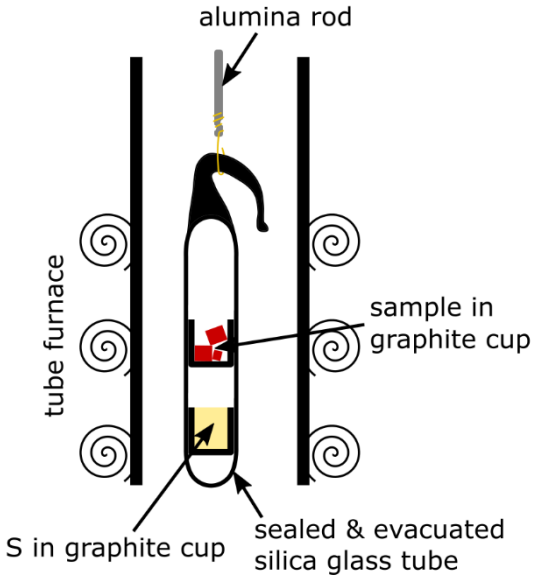

Figure 1: Experimental set-up of the silicate mineral and Mercury glass samples in an evacuated (10^{-5} bar) and sealed silica glass ampule, suspended in a vertical tube furnace. This drawing is modified from Renggli et al. 2022.

In addition to the synthetic Mercury glass samples, we conducted sulfidation experiments with three natural rock-forming minerals. These mineral phases are included in the MERTIS sample database, which is developed in context of the ESA/JAXA BepiColombo mission to Mercury, and were previously characterized chemically by electron microprobe analyzer (EMPA) and mid-IR spectroscopy (Hiesinger et al., 2020). The three mineral phases used in the sulfidation experiments are olivine (ID 135), diopside (ID 134), and anorthite (ID 1). The olivine (ID 135) has a forsterite content of 90.5% (Table 1). The sample ID 135 contains two minor contaminants (<5 vol%.) that are not detectable in the bulk FTIR spectrum of the unreacted material. However, in the SEM we were able to identify the contaminants, which are a diopside and a Cr-Mg hercynite ("picotite", 33.4 wt.% Al_2O_3, 33.2 wt. Cr_2O_3, 17.2 wt. % MgO, 14.1 wt. FeO). The diopside (ID 134) was previously described and studied spectroscopically for its trace water contents (Kumamoto et al., 2017) and has a minor FeO content of ~6.6 wt. % (Table 1). The anorthite contains minor impurities on a grain-scale including alkali feldspar

and a hydrous phase (see electron microprobe supplement). In Table 2 we list the ID numbers of the starting materials and the reaction products.

The sulfidation experiments were conducted in sealed and evacuated silica glass ampules (Figure 1) which were short enough (~4 cm) to fit in the hot zone of the furnace with a length of ~6 cm (C. J. Renggli & Klemme, 2020). The set-up consists of two graphite cups placed above each other in the ampule (wall thickness of 1 mm), with the lower cup filled with elemental S (~0.0015g), and the upper cup filled with the sample material. In previous experiments on the sulfidation of glasses with Mercury compositions we used SiO_2 glass wool to separate the two cups (C.J. Renggli et al., 2022). However, we determined that the addition of the glass wool separator was not necessary but a potential source of sample contamination. Therefore, we did not use glass wool in the experimental set-up for the olivine, diopside, and anorthite sulfidation experiments (Figure 1). After loading the glass tubes, they were sealed under a vacuum of 10^{-5} bar. At experimental temperatures the elemental S forms a gas phase that reacts with the silicate sample. The fO_2 was controlled at the graphite-CO buffer due to the presence of the graphite cups (C. J. Renggli & Klemme, 2021).

Table 1: Major oxide compositions (wt.%) of the three glasses lMgII A, hMgl, and hAl (Morlok et al., 2021; C.J. Renggli et al., 2022), and the minerals olivine, diopside (Kumamoto et al. 2017), and anorthite used in the sulfidation experiments.

	lMgII A ID174	hMgI ID156	hAl ID155	Olivine ID135	Diopside ID134	Anorthite ID1
	Morlok et al., 2021; Renggli et al., 2022			n=20	Kumamoto et al. 2017	n=20
SiO_2	64.26(32)	56.01(38)	57.06(19)	41.04(34)	53.67(09)	43.09(16)
TiO_2	0.46(02)	1.08(01)	1.39(08)	b.d.l.	0.08(01)	b.d.l.
Al_2O_3	14.30(10)	10.80(14)	16.55(11)	-	0.21(06)	36.18(13)
FeO	0.05(08)	b.d.l.	0.07(03)	9.21(12)	6.62(04)	0.04(02)
MnO	0.16(02)	0.49(01)	0.70(04)	0.16(03)	0.55(18)	b.d.l.
MgO	8.97(12)	23.11(45)	14.78(15)	59.17(21)	14.06(24)	b.d.l.
CaO	6.81(08)	7.73(09)	6.05(10)	0.05(02)	25.35(18)	20.28(18)
Na_2O	4.81(12)	1.16(02)	3.15(08)	-	0.04(01)	b.d.l.
K_2O	0.19(03)	0.13(02)	0.24(02)	-	-	b.d.l.
Total	100.01	100.52	99.99	100.04	100.63	99.64

Table 2: ID numbers given to the starting materials and the experiments at 800, 1000, and 1200 °C. These ID numbers refer to the IRIS MERTIS database where the corresponding bulk and in-situ FTIR spectra are available (http://bc-mertis-pi.uni-muenster.de).

material name	ID of starting material	ID experiment 800 °C	ID experiment 1000 °C	ID experiment 1200 °C
Olivine	135	440	441	442
Diopside	134	443	444	445
Anorthite	1	446	447	448
hMgI	156	449	450	451
hMgII	181	452	453	454
lMgII A	174	455	456	457
hAl	155	458	459	460

Analytical methods

The samples retrieved from the quenched silica glass ampules were split in two aliquots. The first aliquot included larger grains that were first used to characterize the surfaces by Scanning Electron Microscopy (SEM) and in-situ characterization by electron microprobe and FTIR microscopy of sample cross-sections. The second aliquot was retained as a powder with unknown grain-size distribution and used for FTIR bulk powder analysis.

Back-scattered electron (BSE) images were made on a JSM-6510 Series SEM in low-vacuum mode at 50 Pa, which allowed imaging without carbon coating. The grains were then embedded in

epoxy resin and polished under anhydrous ethanol, with a final polish using 0.25 µm diamond paste. The chemistry of the reaction products was determined with a JEOL JXA 8530F electron microprobe at 15 keV and 60 nA probe current. The spot size varied depending on grain-size from 1-10 µm. For details on standardization and reference materials we refer to the supplementary material in Renggli et al. (2022).

The bulk and in-situ FTIR reflectance spectra were recorded with a Bruker Hyperion 3000 microscope using a liquid nitrogen cooled MCT detector over a spectral range of 4000 – 600 cm^{-1} at a spectral resolution of 4 cm^{-1}. In this study we discuss the features over the spectral range of 1300 – 800 cm^{-1} and the reported spectra are the averages of 64 or 128 scans. For the bulk measurements the samples were ground dry for less than 30 seconds and placed in Al-metal sample cups. The bulk measurements were done on these powders with an aperture cross-section of 600x600 µm. For the in-situ measurements the microscope aperture was varied depending on the target sample, with the smallest used aperture size of 15x15 µm. The aperture sizes for all in-situ measurements are given with the full spectral data in the electronic supplement, and analysis locations are shown in the BSE images of the respective samples. For bulk spectra we used a gold mirror standard and for the bulk measurements we used an InfraGold diffuse scattering standard.

Experimental results

Reacted surface

The sulfidation of silicates is strongly temperature dependent, due to the diffusion-controlled mobility of the sulfide forming cations (e.g. Fe, Ca, Mg, ±Mn, ±Ti, ±Na) (Renggli, King, et al., 2019; C.J. Renggli et al., 2022). Consequently, the coatings on the reacted samples vary in texture with time, temperature, and silicate composition and structure. In Figure 2 we show BSE images of the surfaces of the 6 types of investigated samples, reacted for 24 h at 1000 °C. The reacted minerals (a-c) show a less complete sulfide coating compared to the reacted glasses (d-f). The sulfide compositions labelled on the BSE images were determined using qualitative EDS in the SEM low-vacuum mode. The detailed sulfide compositions were analyzed by EPMA and are reported in Figure 3 and the supplement.

On the olivine grain sulfidized at 1000 °C we observe two sulfide compositions (Figure 2a), including MgS (niningerite) with grain sizes of up to 8 µm, and (Fe,Mg)S, which appears white in the BSE image, and forms slightly larger grains. The sulfidized diopside is coated by three distinct sulfide phases. First, (Mg,Ca,Fe)S forms the larges grains (<20 µm), second, a Ti-bearing sulfide forms platy grains, and third, (Ca,Mg)S forms smaller grains with diameters <10 µm (Figure 2b). The anorthite has a very un-even coating with parts of the surface entirely coated by CaS, whereas other areas show no sulfide coatings. The CaS only occurs on the anorthite component of the grain, whereas the impurity, an alkali feldspar, shows no sulfide coating. In addition, the textures reveal that the anorthite experienced partial melting, apparent in the lower right corner of the BSE image (Figure 2c). The textures in the coatings of the sulfidized glasses are reported in detail in Renggli et al. (2022). Here, we show the BSE images (Figure 2d-e) to allow a comparison with the mineral experiments. Overall, the sulfides on the glasses show a more diverse chemistry, including Mn, Fe, Na and Ti in predominantly CaS and MgS phases, and the coatings are overall less patchy compared to the minerals. In addition, we observe occasional graphite grains on these surfaces, which are contamination from the graphite cups in which the samples were placed. Since we used SiO_2 glass wool as a spacer in the ampules for the glass sulfidation experiments we looked for traces of this material but did not identify any contamination.

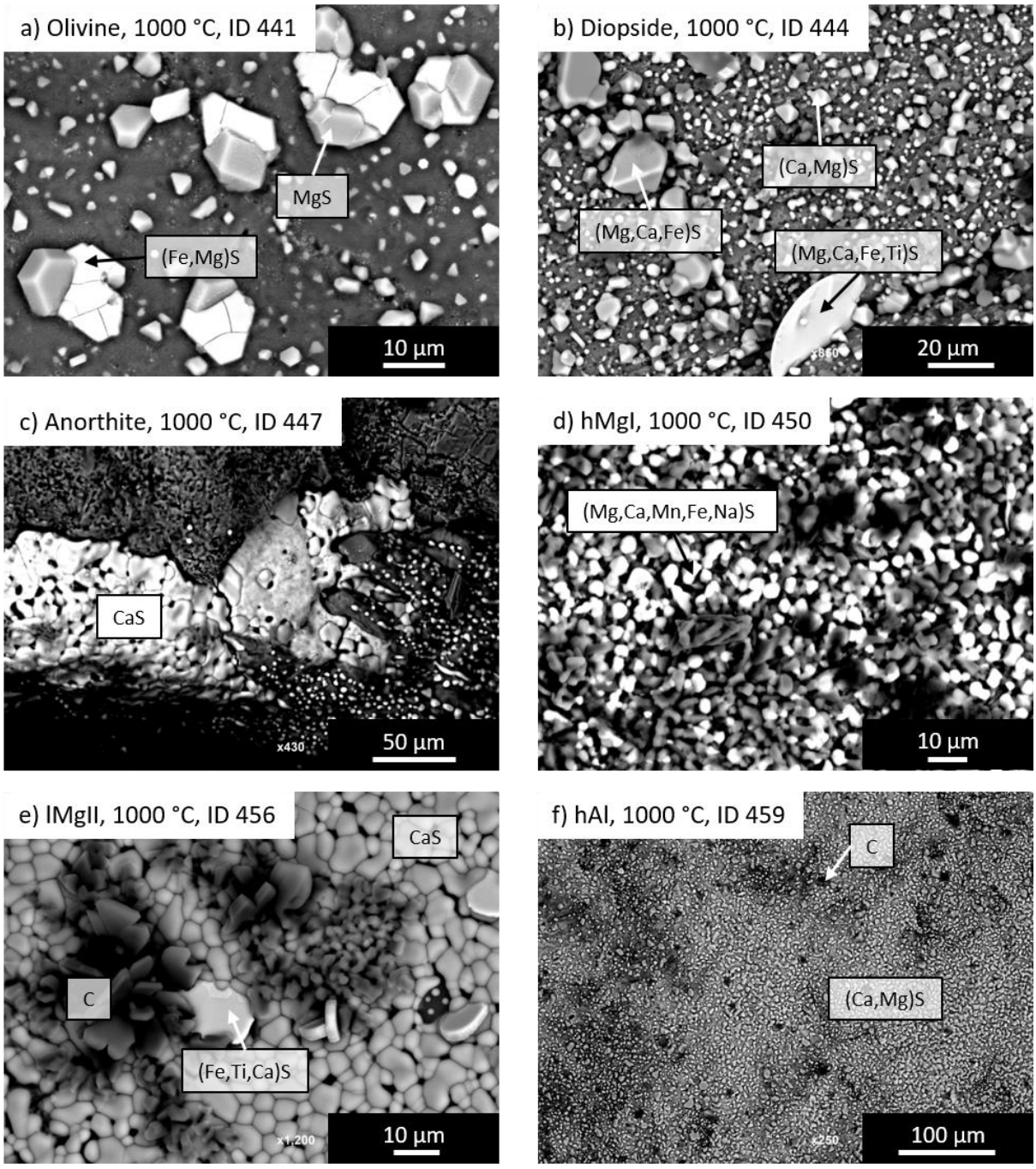

Figure 2: Secondary backscattered electron microscopy images of mineral and glass grains sulfidized for 24 h at 1000 °C. a) olivine ID 441, b) diopside ID 444, c) anorthite ID 447, d) high-Mg glass ID 450, e) low-Mg glass ID 456, f) high-Al glass ID 459. The sulfide coatings are labeled on the images and include MgS, FeS, CaS, and mixed sulfide compositions. For a detailed description of sulfide reaction products in the glass sulfidation experiments we refer the reader to Renggli et al. 2022.

Sulfide compositions

We observe exclusively CaS (oldhamite) on the sulfidized anorthite grains. In contrast, the compositions of the sulfides formed in olivine and diopside sulfidation experiments are compositionally more diverse and vary with experimental temperature from 800 to 1200 °C. In Figure 3 we show the compositional variations of the sulfides on the reacted olivines and diopsides. At 800 °C, the coating on the olivine grains consists of Fe-depleted troilite ($Fe_{1-x}S$). This is compositionally removed from the olivine composition ($Mg_{1.83}Fe_{0.17}SiO_4$, Table 1). However, the Mg/Fe ratio of the sulfide composition (Mg,Fe)S approaches the Mg/Fe ratio of the educt olivine with increasing experimental temperature and degree of sulfidation (Figure 3a). Similarly, the sulfide reaction products on the diopside grains approach the Ca-Mg-(Fe+Ti) molar composition of the unreacted diopside. At 800 °C we observe $(Fe,Ti)_{1-x}S$ and CaS, whereas at higher temperatures (1000 and 1200 °) we also observe Mg-rich (Mg,Ca)S in addition to a Ca-rich sulfide (Figure 3b). We reported the compositions of the sulfides in the glass sulfidation experiments previously (Renggli et al., 2022). We observed similar variations in the Ca-Mg-(Fe+Ti) compositional space in the glass experiments as in the sulfidation of the diopside (Figure 3b). The sulfides in the high-Mg and high-Al glass experiments fell predominantly in the CaS-MgS compositional spaces, whereas we observed abundant Fe-rich and Mg-poor sulfides in the low-Mg glass experiment (Renggli et al., 2022).

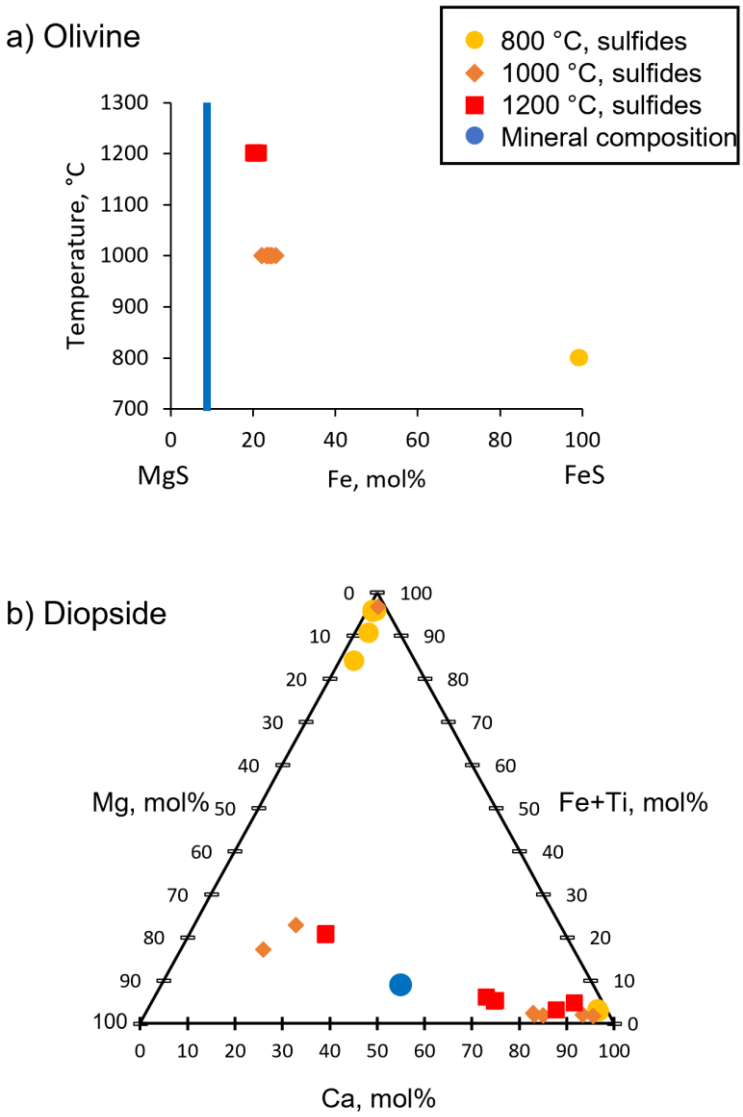

217

218 *Figure 3: Compositions of the sulfides formed in the reactions with a) olivine, and b) diopside. The*
219 *yellow circles show the sulfide compositions of experiments at 800 °C, red diamonds at 1000 °C, and dark red*
220 *squares at 1200 °C. The blue line in a) and the blue circle in b) indicate the compositions of the respective silicate*
221 *starting material.*

Bulk FTIR of reacted surfaces

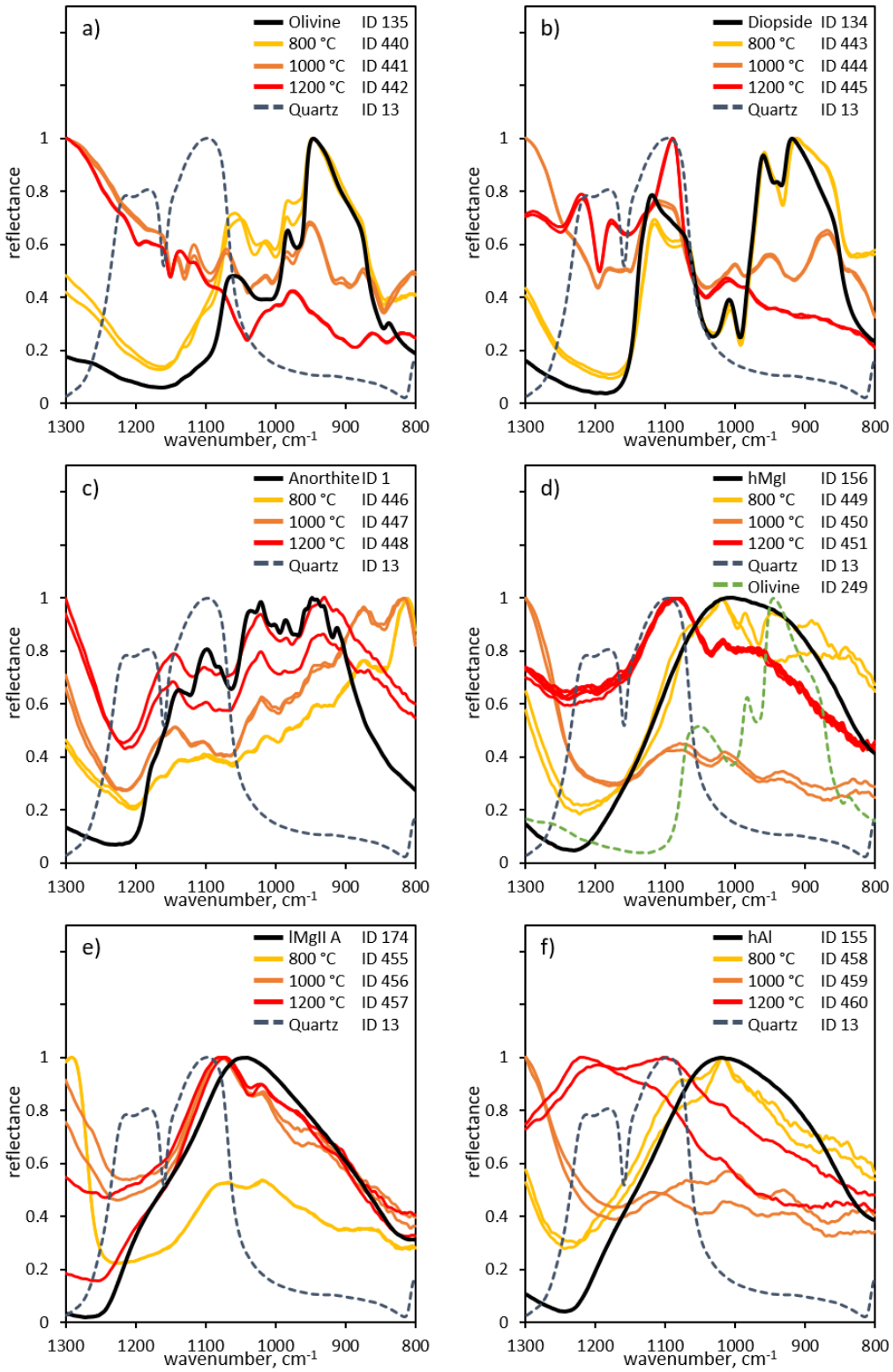

Figure 4: Bulk mid-FTIR spectra of the reacted samples. a) olivine ID 135, b) diopside ID 134, c) anorthite ID 1, d) hMgI ID 156, e) lMgII A ID 174, f) hAl ID 155. The solid black line is the bulk spectrum of the unreacted starting material, the dashed grey line is the spectrum of quartz ID13, and the dashed green line in (d) the spectrum of olivine ID249.

We measured the mid-IR reflectance spectra of the experimental run products over a spectral range of 800 – 1300 cm^{-1} (12.5 – 7.7 μm) to test the effect of mineral and glass sulfidation on the spectral properties (Figure 4). The spectral positions of the reflectance minima (Christiansen Feature, CF) and the reflectance maxima (e.g., Reststrahlenband, RB) of the starting materials are reported in Table 3. Changes in the spectral features represent changes in the sample mineralogy and will be used as a basis to test the sulfidation hypothesis for S-enrichment on the surface of Mercury with the MERTIS instrument onboard BepiColombo. The degree of change in the spectra is strongly dependent on the degree of sulfidation and change in mineralogy, which increases with temperature from 800 to 1200 °C. The sulfidation reaction (Equation 1) predicts the formation of SiO_2 as a reaction product in addition to sulfides. To test for the presence of quartz in the reaction products we show a quartz spectrum (ID 13) in the panels of Figure 4. The three primary RBs are at 1096, 1181, and 1212 cm^{-1}.

Olivine has four RBs with decreasing reflectance at 946, 983, 1060, and 839 cm^{-1}. In the sulfidation experiment at 800 °C the relative intensities of these reflectance RBs largely remain unchanged (Figure 4a). At higher temperatures (1000, 1200 °C) the reflectance of the reacted sample decreases dramatically, and the reflectance maxima of the normalized spectra are at 1300 cm^{-1}. In addition, the high-temperature spectra are noisier compared to that of the 800 °C experiment, or the unreacted olivine. We observe no clear spectral features that we can attribute to quartz.

Diopside (ID 134) has four major RBs with decreasing reflectance at 918, 959, 1119, and 1008 cm^{-1}, a small RB, almost completely overlapped by the two main RBs, at 940 cm^{-1}, and a prominent shoulder at ~1075 cm^{-1} (Figure 4b). The more extensive sulfidation of diopside compared to olivine observed in the SEM images (Figure 2) is also apparent in the bulk FTIR spectra of the diopside reaction products. At 800 °C, where the degree of sulfidation is low, the spectrum retains the primary features of the unreacted diopside. However, at 1000 and 1200 °C the overall reflectance amplitude decreases, but we can also identify the appearance of RBs characteristic for quartz, most prominently at ~1090 cm^{-1} (Figure 4b). At this wavenumber a shoulder appears in the spectra of the experiment at 1000 °C, but becomes the main RB at 1200 °C. Similarly, shoulders and RBs attributable to quartz occur ~1220 cm^{-1} and 1178 cm^{-1}. These RB wavenumbers are within 8 cm^{-1} of the quartz ID 13 reference spectrum, but

255 are not perfect matches. However, vibrational modes are defined by crystallographic structure and
256 record variations in crystal orientation, defect populations, impurities in the reference quartz, or the
257 high-temperature formation conditions in the sulfidation experiments.

258 Anorthite (ID 1) has a complex mid-IR reflectance spectrum, with reflectance maxima at 948,
259 1021, 1036, 985, 914, 1099, 1081, and 1139 cm^{-1} in order of decreasing reflectance. The reflectance
260 minimum CF of anorthite is located at ~1230 cm^{-1}, at higher wavenumbers compared to olivine or
261 diopside (Figure 4c). The presence of RBs at high wavenumbers, in the range of the main quartz RB at
262 ~1100 cm^{-1} may pose a challenge to the identification of sulfidation reaction products in the mid-IR
263 spectra. A further challenge is the mineralogical heterogeneity of the anorthite sample (ID 1) used for
264 this study (see above). The experimental run products are much darker in appearance compared to the
265 starting material. Similarly, the overall reflectance of all experiments has decreased compared to ID 1
266 (Figure 4c). We observe no other spectral signatures of sulfidation in the mid-IR of the anorthite
267 sulfidation experiments.

268 The mid-IR spectra of the synthetic Mercury glasses hMgI (ID 156, Figure 4d), hMgII (ID 181,
269 only in supplement), lMgII A (ID 174, Figure 4e), and hAl (ID 155, Figure 4f) were previously
270 described in Morlok et al. (2021). The glass spectra are characterized by a reflectance minimum (CF)
271 at low wavenumbers, and a broad reflectance maximum (Table 3). The mid-IR spectra of the sulfidized
272 glasses show clear evidence for alteration, and crystallization (Figure 4d-f). In our previous study we
273 have shown that the glasses partially crystallized in the experiments. The hMgI glass formed forsterite
274 and enstatite, the lMgII A glass formed forsterite, and the hAl glass formed plagioclase and Mg-rich
275 clinopyroxene (Renggli et al. 2022). The sulfidation removed Ca and Mg from the glass and enriched
276 the altered substrate glass in SiO_2. The main band position shifts to higher wavenumbers with increasing
277 SiO_2 content (Dufresne et al., 2015; Morlok et al., 2021, 2023), which is apparent in the shift of the
278 main reflectance peak of the most strongly altered experiments at 1200 °C (Figure 4d,e). As in the case
279 of the sulfidized minerals, the overall reflectance is lower in the experiments compared to the unaltered
280 glasses, resulting in noisy mid-IR spectra (e.g. Figure 4f).

281

Table 3: Christiansen Feature (CF) and Reststrahlenband (RB) spectral positions in wavenumber and wavelength for the starting materials. The RBs are ordered by decreasing reflectance. For glasses we only report the spectral position of the reflectance maximum. For more details on the spectral features of the glasses see Morlok et al. (2021).

		Olivine ID 135	Diopside ID 134	Anorthite ID 1	Quartz ID 13	hMg I ID 156	hMg II ID 181	lMg IIA ID 174	hAl ID 155
CF		1163 cm^{-1} *8.60 µm*	1184 cm^{-1} *8.44 µm*	1229 cm^{-1} *8.13 µm*	1354 cm^{-1} *7.39 µm*	1229 cm^{-1} *8.13 µm*	1242 cm^{-1} *8.05 µm*	1268 cm^{-1} *7.89 µm*	1242 cm^{-1} *8.05 µm*
RB	1	946 cm^{-1} *10.57 µm*	918 cm^{-1} *10.89 µm*	948 cm^{-1} *10.54 µm*	1096 cm^{-1} *9.12 µm*	1005 cm^{-1} *9.95 µm*	1021 cm^{-1} *9.79 µm*	1045 cm^{-1} *9.57 µm*	1019 cm^{-1} *9.81 µm*
	2	983 cm^{-1} *10.18 µm*	959 cm^{-1} *10.43 µm*	1021 cm^{-1} *9.79 µm*	1181 cm^{-1} *8.47 µm*				
	3	1060 cm^{-1} *9.43 µm*	940 cm^{-1} *10.64 µm*	1036 cm^{-1} *9.65 µm*	1212 cm^{-1} *8.25 µm*				
	4	839 cm^{-1} *11.92 µm*	1119 cm^{-1} *8.94 µm*	985 cm^{-1} *10.15 µm*					
	5		1075 cm^{-1} *9.30 µm*	914 cm^{-1} *10.94 µm*					
	6		1008 cm^{-1} *9.92 µm*	1099 cm^{-1} *9.10 µm*					
	7			1081 cm^{-1} *9.25 µm*					
	8			1139 cm^{-1} *8.78 µm*					

In-Situ investigations

We report observations of cross-sectioned experimental samples, including SEM images and in-situ micro-FTIR spectra (Figures 5-10). Sulfidation is not limited to the surface of the mineral grains, but also occurs in cracks. These cracks were likely present in the grains prior to the experiments. The BSE images show changes in the silicate substrates and micro-FTIR measurement areas are indicated as blue rectangles. The dimensions of these measurement areas are approximate and reported in detail in the supplement with the micro-FTIR spectral data. Here, we describe the spectral features of the sulfidized mineral and glass grains.

The in-situ observations of the sulfidized olivine (ID 135) reacted at 1000 °C (ID 441) and 1200 °C (ID 442) are shown in Figure 5. The grain in Figure 5b was only polished superficially and not to the core of the grain. The spectra on the sample reacted at 1000 °C (Figure 5a), therefore represent those of the altered near-surface area. Nevertheless, these spectra are very similar to the unaltered olivine. An additional strong RB is apparent in the spectrum of area 2 at 1082 cm^{-1}. Similarly, the sulfidation of olivine at 1200 °C has not progressed sufficiently to result in a change in mineralogy (e.g. formation of quartz), and the mid-IR spectra remain characteristic for olivine (Figure 5c). Notably,

sulfidation has occurred in thin cracks within the olivine grain, and the BSE image shows a gray-scale gradient towards the grain surface, indicative for diffusional loss of Fe to the sulfide (Figure 5d).

The surface SEM observations suggest a higher rate of sulfidation for diopside, compared to olivine (Figure 2). This observation is also supported by the in-situ investigations. At 1000 °C little alteration can be observed (Figure 6b) and the micro-FTIR spectra show no change from diopside (Figure 6a). However, at 1200 °C strong sulfidation is evident in the BSE image of the sample cross-section (Figure 6d). The sulfidation reaction has extended into cracks by up to 200 µm. The cracks are widened and filled by (Ca,Mg)S and quartz (darker gray compared to diopside in Figure 6d). The spectra recorded over the cracks (1-4), however, show limited changes compared to the unreacted diopside. The overall reflectance of these spectra is low and they appear noisy. Despite the presence of quartz, observed by SEM, no clear quartz RBs are evident. Instead, the spectral signature of the diopside dominates the spectra (Figure 6c).

In-situ observations of sulfidized anorthite are limited to the experiment at 1200 °C (Figure 7), due to the heterogeneity of the starting material. The BSE image shows pervasive sulfidation, even in the interior of the sample (Figure 7b). The sample has partially molten and quench crystals can be observed. The partially glassy nature of the sample is apparent in the micro-FTIR spectrum of the area labelled “altered”, as a broad band, reminiscent of the FTIR spectra of the unaltered glasses (Figure 4).

The high-Mg glass (hMgI, ID 156) has crystallized forsterite in the substrate at 800 °C (Figure 8b). Additionally, we observe Fe metal nuggets in the substrate which formed in the synthesis of the glass used in the sulfidation experiments, because the FeO-content was too high for the imposed fO_2 (Morlok et al., 2021). The forsterite is clearly identified in the micro-FTIR spectra of the sample interior (dotted lines, Figure 8a). At 1200 °C the only phase that crystallized in the substrate during the experiment was enstatite, due to the loss of Mg to (Mg,Ca)S in the coating (Renggli et al., 2022). However, even though the enstatite was identified in the sample by electron microprobe analysis, the mid-IR spectrum of the enstatite-rich sample interior remains ambiguous. The enstatite reference material ID 53 (Weber et al., 2020), a bulk powder sample in the grain-size range of 63-125 µm, has two RBs at high wavenumbers (1099 cm^{-1} & 1060 cm^{-1}), where the experimental spectrum has only one

(1084 cm^{-1}), and similarly three RBs at lower wavenumbers in ID 53 (978 cm^{-1}, 957 cm^{-1}, 929 cm^{-1}), where the experimental sample has a very broad RB at 949 cm^{-1}. This difference is likely due to differences in crystal grain orientation (Tappert et al., 2013). At the surface the sample is strongly Mg-depleted (Renggli et al., 2022). Surface spectrum 1 (Figure 8d) shows an enstatite band at 1005 cm^{-1}, whereas the surface spectra 2 and 3 show now enstatite and the main reflectance maxima are shifted to higher wavenumbers. Despite the abundant presence of (Mg,Ca)S in the sample area recorded by surface spectrum 2 (Figure 8e), there is no evidence for a spectral signature of the sulfide.

In Figure 9, we show the in-situ observations of the experiments with the low-Mg glass (lMgII A, ID 174) at 1000 °C (Figure 9a, b) and 1200 °C (Figure 9c, d). At 1000 °C, the sulfide coating, consisting primarily of CaS (Renggli et al., 2022), was thick enough to allow a micro-IR measurement of the sulfide only, shown as #2 in Figure 9a. The CaS spectrum is very noisy and the reflectance maximum was normalized to 1. The reflectance maximum of "surf. 2" is at ~1082 cm^{-1}, which is in the same spectral range as the surface areas including the substrate ("surf. 1" at 1070 and "surf. 3" at 1072 cm^{-1}). However, the absolute reflectance maximum of the CaS spectrum ("surf. 2") is at 0.03, compared to 0.14 for "surf. 3", and 0.18 for "surf. 4", measured with the same aperture size of 20x20 µm. Similarly, the reflectance spectra measured on the large (Ca,Mg)S grains in the experiment at 1200 °C (Figure 9d) have very low absolute mid-IR reflectance values and are only reported in the supplement. Figure 9c shows the clear identification of quartz, crystallizing from the sulfidized glass, in the mid-IR.

The high-Al glass (hAl, ID 155) did not crystallize at 800 °C (Figure 10d). Sulfidation extends into thin cracks. However, we observe no change in the mid-IR reflectance spectra measured along the cracks (Figure 10a), except for a decrease in overall reflectance and increase in spectral noise. At 1200 °C the sulfidation formed a thick coating of (Mg,Ca)S, and the interior of the sample crystallized plagioclase and Mg-rich Cpx (Renggli et al., 2022, Figure 10d). The mid-IR reflectance spectra recorded at the sulfidized sample surface show now sulfide signal, but a shift of the reflectance maximum to higher wavenumbers (Figure 10c).

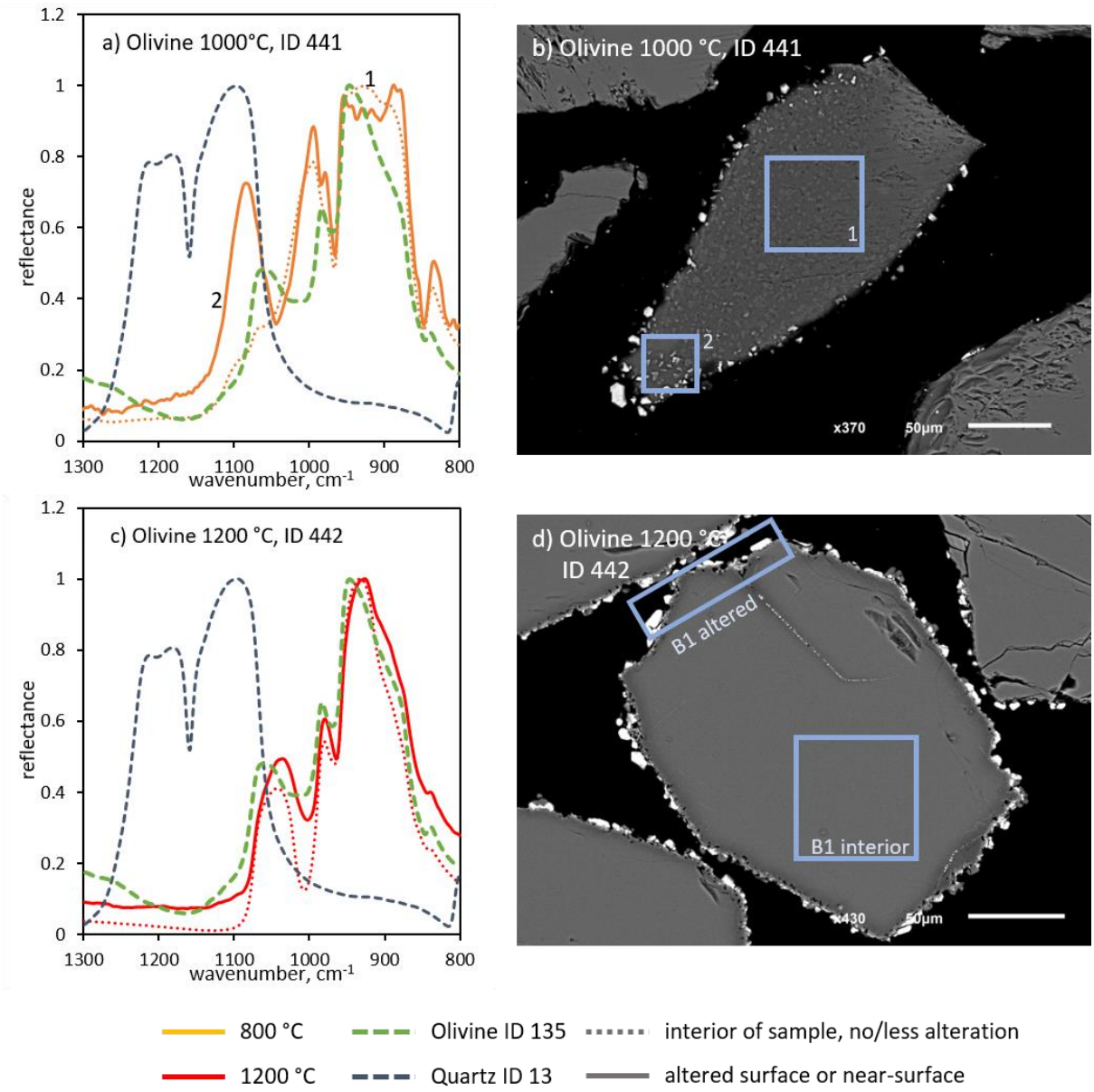

354

355 *Figure 5: In-situ micro-FTIR observations of the reacted olivine (ID 135) and BSE images of the sample*
356 *cross-sections and measurement locations. (a & b) experiment at 1000 °C, ID 441; (c & d) experiment at 1200 °C,*
357 *ID 442. Solid lines indicate spectra recorded at or near the altered surface of the grain, dotted lines are spectra*
358 *of the unaltered interiors of the samples, dashed lines are the bulk spectra of reference phases. The blue boxes*
359 *indicate the areas where the in-situ spectra were recorded.*

360

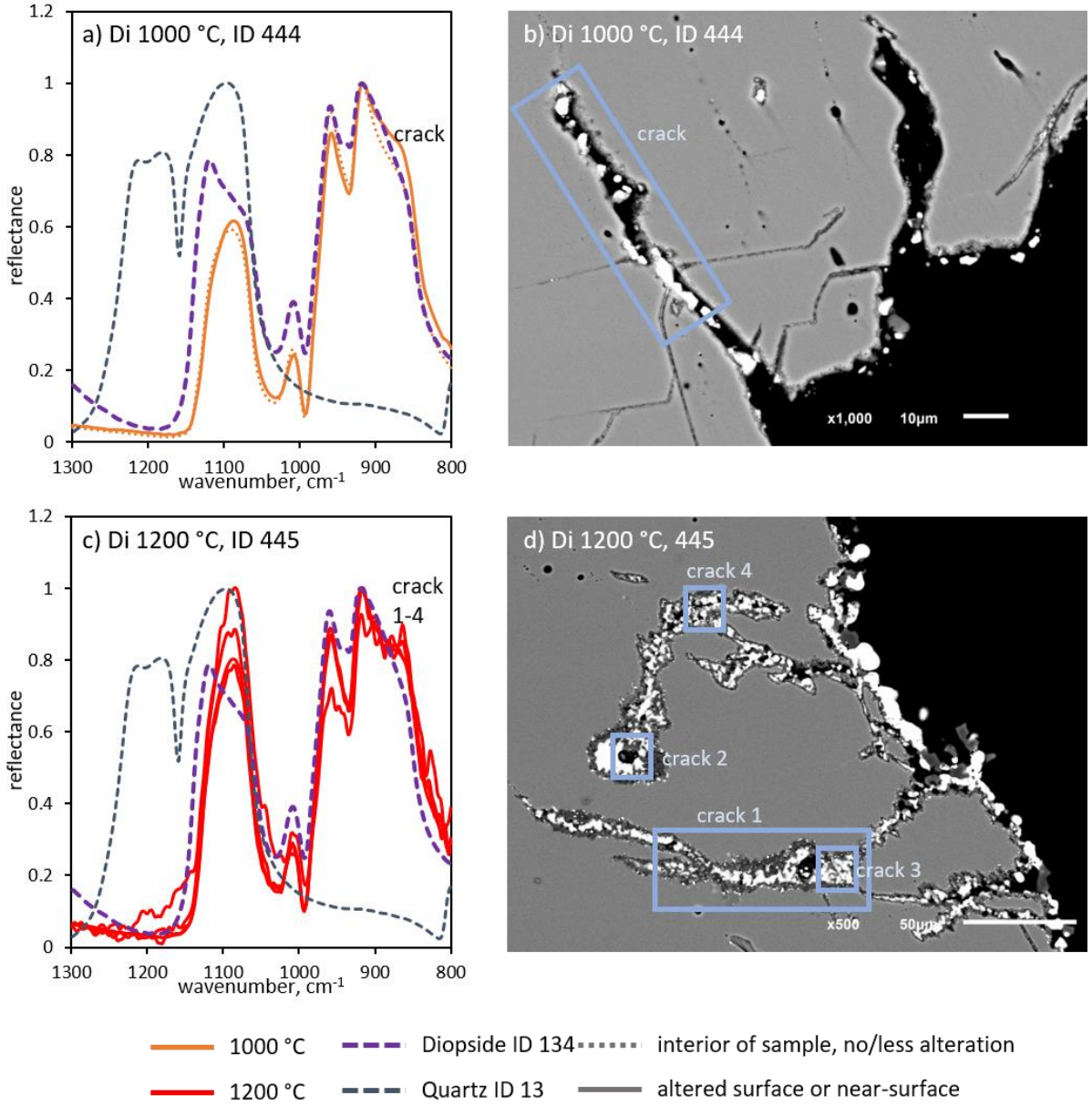

361

362 *Figure 6: In-situ micro-FTIR observations of the reacted diopside (ID 134) and BSE images of the*
363 *sample cross-sections and measurement locations. (a & b) experiment at 1000 °C, ID 444; (c & d) experiment at*
364 *1200 °C, ID 445. Solid lines indicate spectra recorded at or near the altered surface of the grain, dotted lines are*
365 *spectra of the unaltered interiors of the samples, dashed lines are the bulk spectra of reference phases. The blue*
366 *boxes indicate the areas where the in-situ spectra were recorded.*

367

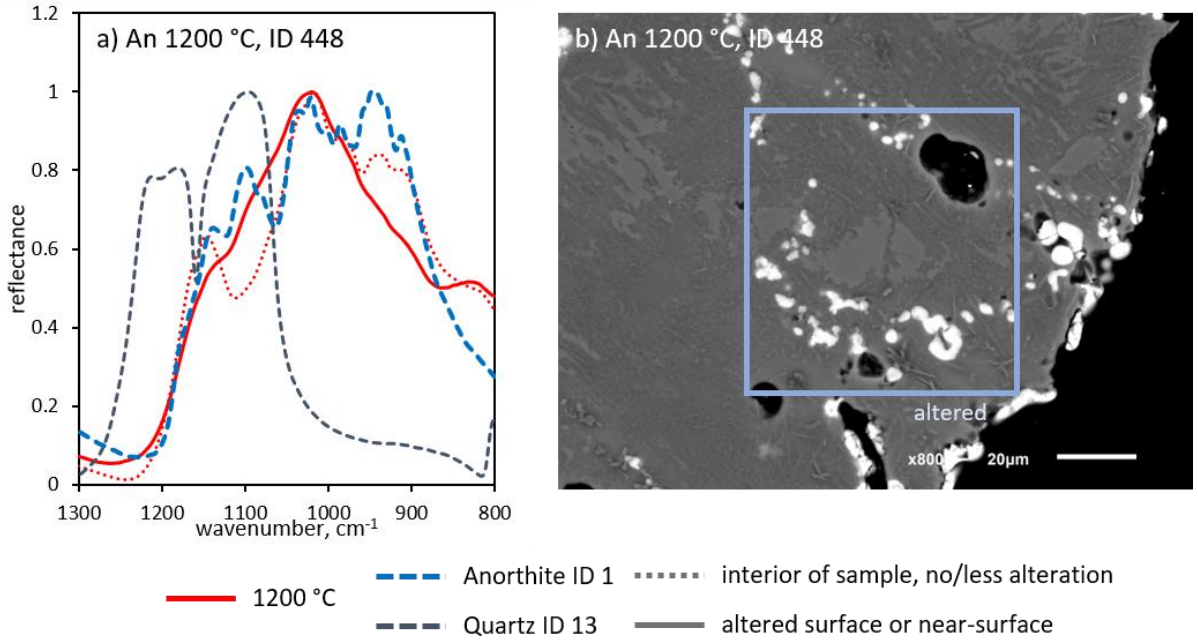

368

369 *Figure 7: In-situ micro-FTIR observations of the reacted anorthite (ID 1) and BSE images of the sample*
370 *cross-sections and measurement locations. (a & b) experiment at 1200 °C, ID 448. Solid lines indicate spectra*
371 *recorded at or near the altered surface of the grain, dotted lines are spectra of the unaltered interiors of the*
372 *samples, dashed lines are the bulk spectra of reference phases. The blue box indicates the area where the in-situ*
373 *spectrum was recorded.*

374

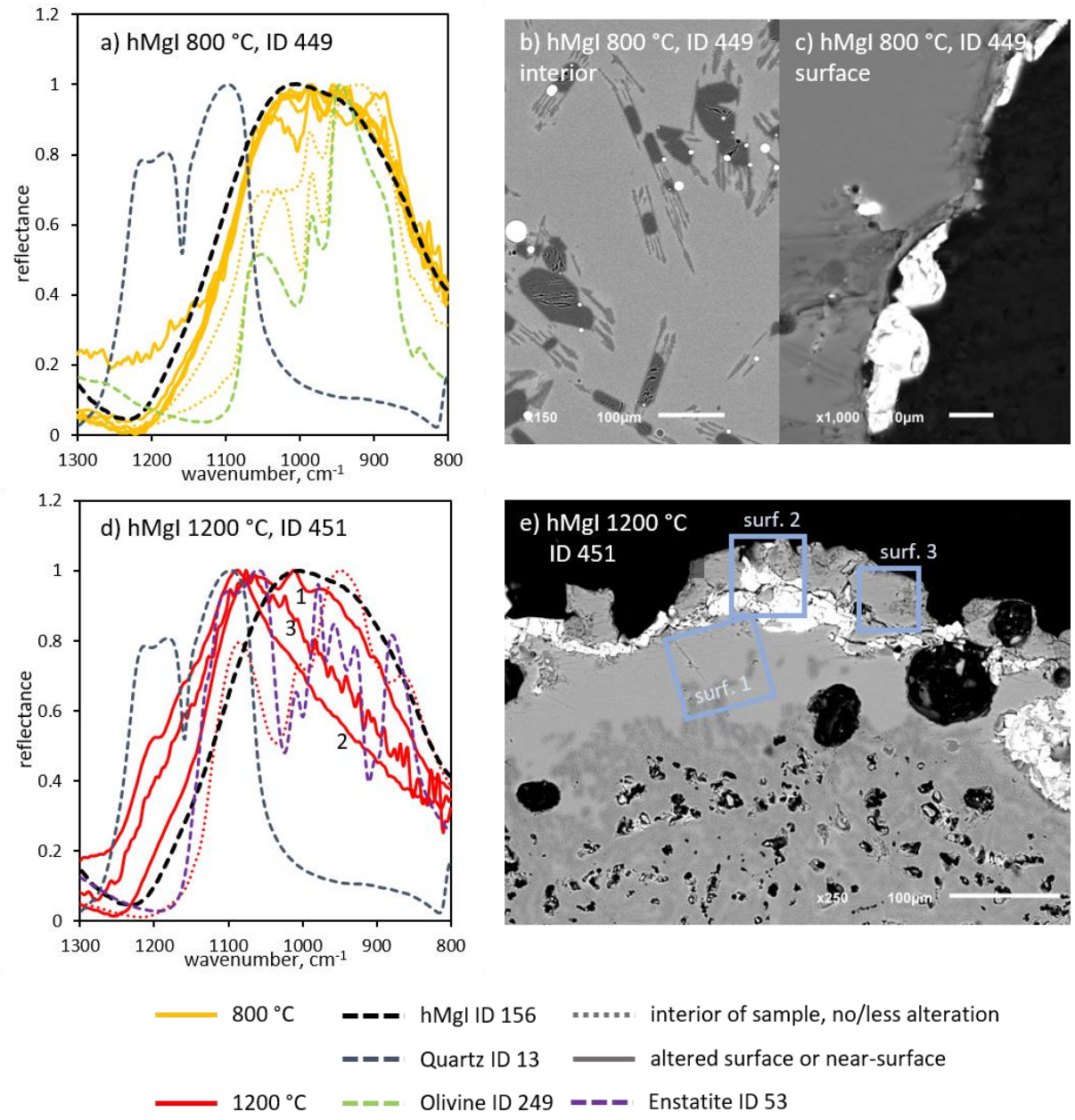

375

376 *Figure 8: In-situ micro-FTIR observations of the reacted high-Mg I glass (ID 156) and BSE images of*
377 *the sample cross-sections and measurement locations. (a - c) experiment at 800 °C, ID 449; (d & e) experiment*
378 *at 1200 °C, ID 451. Solid lines indicate spectra recorded at or near the altered surface of the grain, dotted lines*
379 *are spectra of the unaltered interiors of the samples, dashed lines are the bulk spectra of reference phases. The*
380 *blue boxes indicate the areas where the in-situ spectra were recorded.*

381

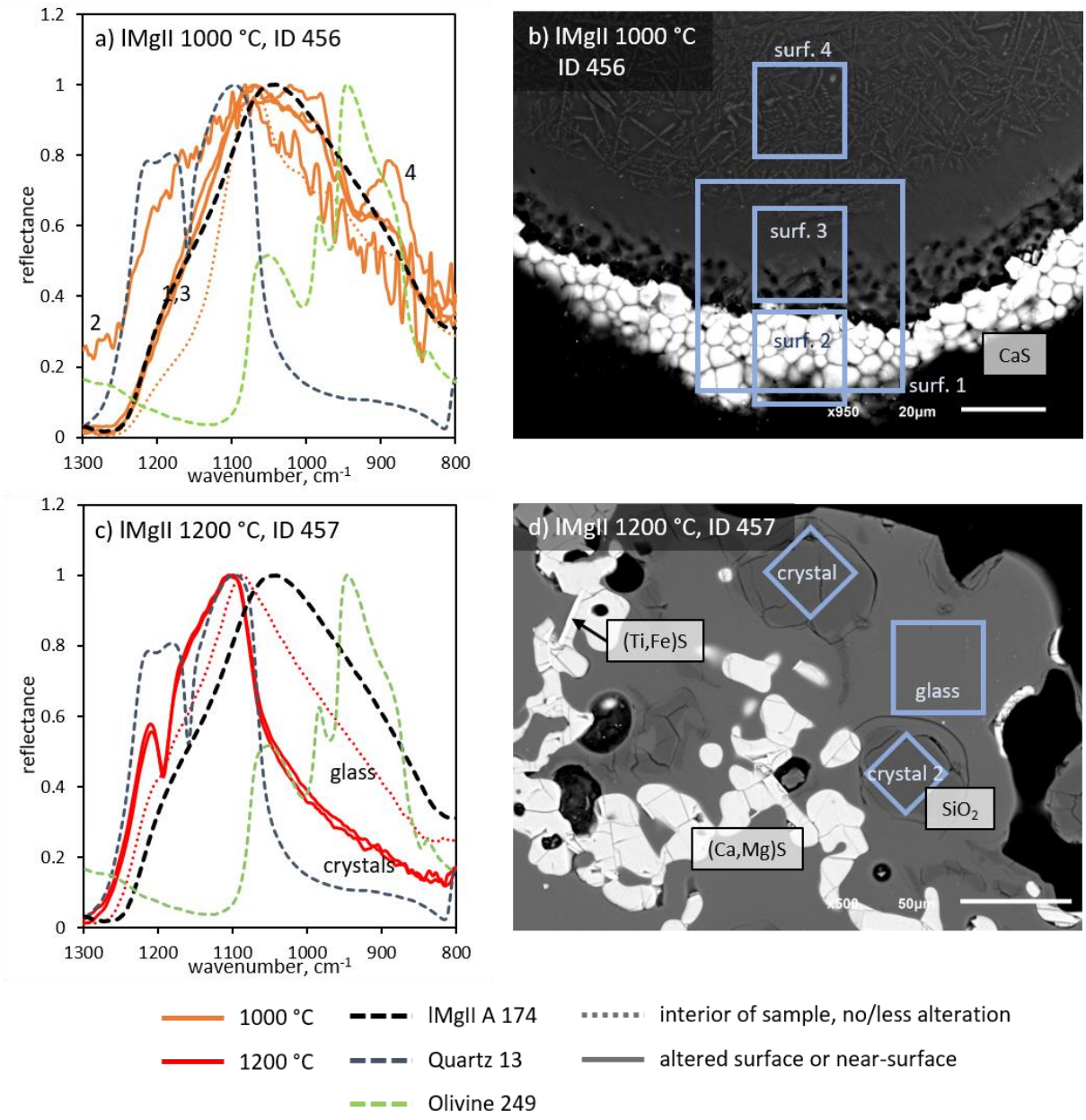

382

383 *Figure 9: In-situ micro-FTIR observations of the reacted low-Mg II A glass (ID 174) and BSE images of*
384 *the sample cross-sections and measurement locations. (a & b) experiment at 1000 °C, ID 456; (c & d) experiment*
385 *at 1200 °C, ID 457. Solid lines indicate spectra recorded at or near the altered surface of the grain, dotted lines*
386 *are spectra of the unaltered interiors of the samples, dashed lines are the bulk spectra of reference phases. The*
387 *blue boxes indicate the areas where the in-situ spectra were recorded.*

388

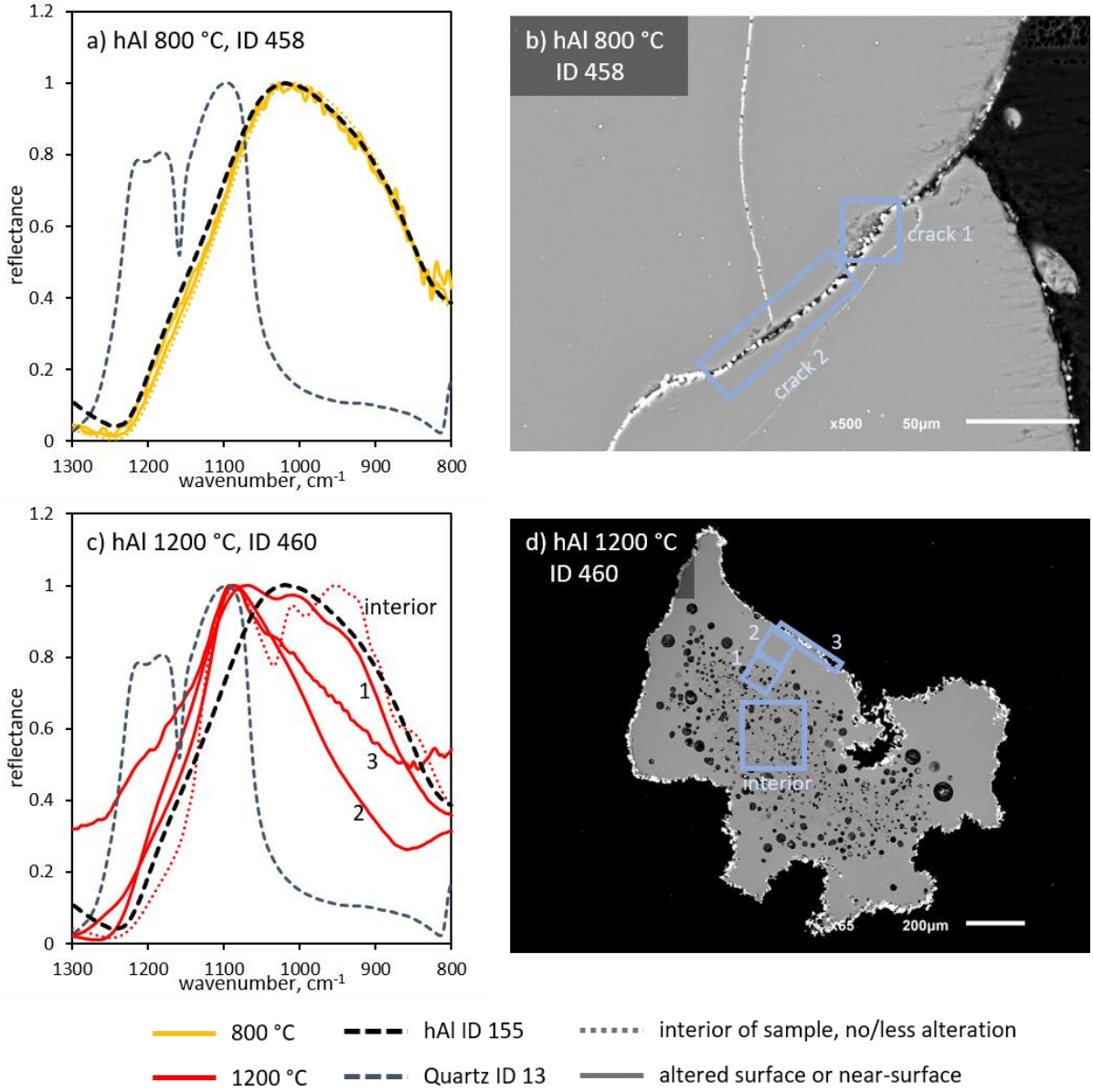

389

390 *Figure 10: In-situ micro-FTIR observations of the reacted high-Al glass (ID 155) and BSE images of the*
391 *sample cross-sections and measurement locations. (a & b) experiment at 800 °C, ID 458; (c & d) experiment at*
392 *1200 °C, ID 460. Solid lines indicate spectra recorded at or near the altered surface of the grain, dotted lines are*
393 *spectra of the unaltered interiors of the samples, dashed lines are the bulk spectra of reference phases. The blue*
394 *boxes indicate the areas where the in-situ spectra were recorded.*

395

396

397

398

399

Discussion

We presented experimental results on sulfidation of minerals and glasses, and the effect of the sulfidation reactions on bulk and in-situ mid-IR spectra. The experiments show a strong temperature dependence of silicate sulfidation, which is controlled by the mobility of sulfide-forming cations. The sulfide coatings on the reacted samples exhibit varying textures depending on temperature, silicate composition and structure (e.g. minerals vs. glasses), and time. The sulfide compositions also vary with temperature and range from troilite and CaS to more diverse compositions containing Mg, Ca, Fe, Ti, Mn, and Na (see also Renggli et al., 2022). The mid-IR reflectance spectra of the experimental run products show changes in their spectral features, in particular, we can identify quartz as a reaction product (e.g. equation 1) spectroscopically. The results of our experiments provide important insights into sulfidation reactions and have implications for understanding the geochemistry of planetary surfaces. We argue that S-rich fumarolic and volcanic gases on Mercury reacted at the planet's surface with silicates in volcanic and regolith materials, and led to the observed (Evans et al., 2012; Larry R. Nittler et al., 2011) S-enrichment on the surface of the planets.

At low fO_2 values elements that normally behave lithophile (Ca, Mg, Ti, Na, and K), bond to S^{2-}, in a pseudo-equilibrium in which S^{2-} replaces O^{2-} in the case of glasses and melts (Fincham & Richardson, 1954; O'Neill & Mavrogenes, 2002). In crystalline phases this change of behavior is expressed in the formation of sulfides such as oldhamite (CaS), niningerite (MgS), or daubréelite ($FeCr_2S_4$) amongst others, which have been predicted to occur on the surface of Mercury (Larry R. Nittler et al., 2011; Weider et al., 2012), and are abundantly observed in enstatite chondrites (Keil, 1968). The high abundance of S on the surface of Mercury measured by MESSENGER, at concentrations of up to 4 wt.% (Evans et al., 2012; Larry R. Nittler et al., 2011), was therefore interpreted to be hosted in magmatic phases at highly reducing conditions (Anzures, Parman, Milliken, Namur, et al., 2020; Namur et al., 2016; Mikhail Y. Zolotov et al., 2013). For example, at 1350-1500 °C, 4 wt.% of S could be dissolved in silicate melts at very reducing conditions of ~IW-6 (Anzures, Parman, Milliken, Namur, et al., 2020; Namur et al., 2016). Yet, the FeO content in surface silicates on Mercury was determined 0.2 to 4.5 wt% (Evans et al., 2012; McClintock et al., 2008; McCoy et al.,

2018), which would be too high for such highly reducing conditions, if the FeO was dissolved in a silicate melt, requiring the presence of Fe in sulfides or a metal phase (Mikhail Y. Zolotov et al., 2013). Further evidence for low fO_2 at the surface of Mercury is the low O/Si (1.2 ± 0.1) ratio measured by Gamma-Ray Spectrometry (Larry R Nittler et al., 2018). However, this low O/Si ratio, observed at the very surface of the planet, may be due to space weathering and graphite-induced smelting reactions (Iacovino et al., 2023; McCubbin et al., 2017). Magmas and gases interacting with graphite would be buffered at the graphite-CO buffer for fO_2 at the low pressure conditions on the surface of Mercury (Keppler & Golabek, 2019). However, since the slope of the graphite-CO buffer in fO_2 vs. temperature is not the same as that of mineral redox buffers, such as IW, it may be more useful fO_2 reference for the surface of Mercury, in particular when referring to gas-solid reactions such as sulfidation or smelting.

Considering these observations and their caveats regarding the surface chemistry of Mercury, it is important to consider alternative mechanisms that may explain the observations. As we have argued previously (Renggli et al., 2022), the sulfidation of silicate minerals and glasses forms quartz as a reaction product in association with sulfides including oldhamite, niningerite, troilite, and solid solutions of sulfides. In the experiments that we present in this study, the formation of quartz is most evident in the rapidly sulfidizing diopside together with (Ca,Mg)S. In the reflectance spectra of the bulk powder samples (Figure 4) we observe the spectral signature of quartz in the diopside sample sulfidized at 1200 °C. In the experiments with glasses we observe a shift of the mid-IR reflectance maximum to higher wavenumbers, due to a relative increase of SiO_2 in the altered material (Figure 4d-f). In contrast, we observe no spectral signature in mid-IR reflectance mode of the sulfides that formed in the experiments, including a spectrum recorded on CaS alone (spectrum “surf. 2” in Figure 9a). The overall mid-IR reflectance of the sulfides targeted in-situ is very low, suggesting a low albedo of the material, perhaps due to the experimental setup in graphite crucibles. This observation is in opposition to a previous study that observed spectral features in mid-IR reflectance and emission for CaS, and a high albedo for a synthetic CaS material (Varatharajan et al., 2019).

In summary, we suggest that the effect of sulfidation and S enrichment on the surface of Mercury by gas-solid reactions will be testable by BepiColombo, using the MERTIS instrument that

observes the planet in the mid-IR spectral range. We expect the identification of quartz to correlate with the surface abundance of sulfides, including oldhamite, niningerite, and troilite. The rates of sulfidation reactions for different mineral phases remain poorly constrained and require further work. We also aim to better constrain the changes in spectral properties of materials as a function of the degree of sulfidation, as a function of time and S abundance, for reflectance and emission spectroscopy.

Acknowledgements

CR is funded by the Deutsche Forschungsgemeinschaft (DFG, German Research Foundation) – project 442083018. This research is partially supported by DFG project 263649064 – SFB TRR170, publication #XYZ. A.N.S., A.M., I.W., and H.H. acknowledge funding from the DLR, grants 50QW1701 and 50QW2201A1302.

Open Research

The spectral data will become available on the Infrared and Raman for Interplanetary Spectroscopy (IRIS) database at http://bc-mertis-pi.uni-muenster.de/ upon acceptance of the manuscript for publication.

References

Anzures, B. A., Parman, S. W., Milliken, R. E., Namur, O., Cartier, C., & Wang, S. (2020). Effect of sulfur speciation on chemical and physical properties of very reduced mercurian melts. *Geochimica et Cosmochimica Acta*, *286*, 1–18. https://doi.org/10.1016/j.gca.2020.07.024

Anzures, B. A., Parman, S. W., Milliken, R. E., Lanzirotti, A., & Newville, M. (2020). XANES spectroscopy of sulfides stable under reducing conditions. *American Mineralogist*, *105*(3), 375–381. https://doi.org/10.2138/am-2020-7146

Cartier, C., Hammouda, T., Doucelance, R., Boyet, M., Devidal, J.-L., & Moine, B. (2014). Experimental study of trace element partitioning between enstatite and melt in enstatite chondrites at low oxygen fugacities and 5GPa. *Geochimica et Cosmochimica Acta*, *130*, 167–187. https://doi.org/10.1016/j.gca.2014.01.002

Deutsch, A. N., Head, J. W., Parman, S. W., Wilson, L., Neumann, G. A., & Lowden, F. (2021). Degassing of volcanic extrusives on Mercury: Potential contributions to transient atmospheres and buried polar deposits. *Earth and Planetary Science Letters*, *564*, 116907. https://doi.org/10.1016/j.epsl.2021.116907

Dufresne, C. D. M., King, P. L., Dyar, M. D., & Dalby, K. N. (2015). Effect of SiO2, total FeO, Fe3+/Fe2+, and alkali elements in basaltic glasses on mid-infrared. *American Mineralogist*, *94*(11–12), 1580–1590. https://doi.org/10.2138/am.2009.3113

Evans, L. G., Peplowski, P. N., Rhodes, E. A., Lawrence, D. J., McCoy, T. J., Nittler, L. R., et al. (2012). Major-element abundances on the surface of Mercury: Results from the MESSENGER Gamma-Ray Spectrometer. *Journal of Geophysical Research: Planets*, *117*(E12). https://doi.org/10.1029/2012JE004178

Fincham, C. J. B., & Richardson, F. D. (1954). The behaviour of sulphur in silicate and aluminate melts. *Proceedings of the Royal Society of London. Series A. Mathematical and Physical Sciences*, *223*(1152), 40–62. https://doi.org/10.1098/rspa.1954.0099

Foley, S. F. (2011). A Reappraisal of Redox Melting in the Earth's Mantle as a Function of Tectonic Setting and Time. *Journal of Petrology*, *52*(7–8), 1363–1391. https://doi.org/10.1093/petrology/egq061

Hiesinger, H., & Helbert, J. (2010). The Mercury Radiometer and Thermal Infrared Spectrometer (MERTIS) for the BepiColombo mission. *Planetary and Space Science*, *58*(1), 144–165. https://doi.org/10.1016/j.pss.2008.09.019

Hiesinger, H., Helbert, J., Alemanno, G., Bauch, K. E., D'Amore, M., Maturilli, A., et al. (2020). Studying the Composition and Mineralogy of the Hermean Surface with the Mercury Radiometer and Thermal Infrared Spectrometer (MERTIS) for the BepiColombo Mission: An Update. *Space Science Reviews*, *216*(6), 110. https://doi.org/10.1007/s11214-020-00732-4

Iacovino, K., McCubbin, F. M., Vander Kaaden, K. E., Clark, J., Wittmann, A., Jakubek, R. S., et al. (2023). Carbon as a key driver of super-reduced explosive volcanism on Mercury: Evidence from graphite-melt smelting experiments. *Earth and Planetary Science Letters*, *602*, 117908. https://doi.org/10.1016/j.epsl.2022.117908

Keil, K. (1968). Mineralogical and chemical relationships among enstatite chondrites. *Journal of Geophysical Research (1896-1977)*, *73*(22), 6945–6976. https://doi.org/10.1029/JB073i022p06945

Keppler, H., & Golabek, G. (2019). Graphite floatation on a magma ocean and the fate of carbon during core formation. *Geochemical Perspectives Letters*, 12–17. https://doi.org/10.7185/geochemlet.1918

Kerber, L., Head, J. W., Blewett, D. T., Solomon, S. C., Wilson, L., Murchie, S. L., et al. (2011). The global distribution of pyroclastic deposits on Mercury: The view from MESSENGER flybys 1–3. *Planetary and Space Science*, *59*(15), 1895–1909. https://doi.org/10.1016/j.pss.2011.03.020

King, P. L., Wheeler, V. M., Renggli, C. J., Palm, A. B., Wilson, S. A., Harrison, A. L., et al. (2018). Gas–Solid Reactions: Theory, Experiments and Case Studies Relevant to Earth and Planetary Processes. *Reviews in Mineralogy and Geochemistry*, *84*, 1–56.

Kumamoto, K. M., Warren, J. M., & Hauri, E. H. (2017). New SIMS reference materials for measuring water in upper mantle minerals. *American Mineralogist*, *102*(3), 537–547. https://doi.org/10.2138/am-2017-5863CCBYNCND

McClintock, W. E., Izenberg, N. R., Holsclaw, G. M., Blewett, D. T., Domingue, D. L., Head, J. W., et al. (2008). Spectroscopic Observations of Mercury's Surface Reflectance During MESSENGER's First Mercury Flyby. *Science*, *321*(5885), 62–65. https://doi.org/10.1126/science.1159933

McCoy, T. J., Peplowski, P. N., Mccubbin, F. M., Weider, S. Z., Solomon, S. C., Nittler, L. R., & Anderson, B. J. (2018). The Geochemical and Mineralogical Diversity of Mercury. In *Mercury, The View After MESSENGER* (pp. 176–190). Cambridge University Press.

McCubbin, F. M., Vander Kaaden, K. E., Peplowski, P. N., Bell, A. S., Nittler, L. R., Boyce, J. W., et al. (2017). A Low O/Si Ratio on the Surface of Mercury: Evidence for Silicon Smelting? *Journal of Geophysical Research: Planets*, *122*(10), 2017JE005367. https://doi.org/10.1002/2017JE005367

Morlok, A., Renggli, C., Charlier, B., Reitze, M. P., Klemme, S., Namur, O., et al. (2021). Mid-infrared reflectance spectroscopy of synthetic glass analogs for mercury surface studies. *Icarus*, *361*, 114363. https://doi.org/10.1016/j.icarus.2021.114363

Morlok, A., Renggli, C., Charlier, B., Namur, O., Klemme, S., Reitze, M. P., et al. (2023). A mid-infrared study of synthetic glass and crystal mixtures analog to the geochemical terranes on mercury. *Icarus*, *396*, 115498. https://doi.org/10.1016/j.icarus.2023.115498

Namur, O., & Charlier, B. (2017). Silicate mineralogy at the surface of Mercury. *Nature Geoscience*, *10*(1), 9–13. https://doi.org/10.1038/ngeo2860

Namur, O., Charlier, B., Holtz, F., Cartier, C., & McCammon, C. (2016). Sulfur solubility in reduced mafic silicate melts: Implications for the speciation and distribution of sulfur on Mercury. *Earth and Planetary Science Letters*, *448*, 102–114. https://doi.org/10.1016/j.epsl.2016.05.024

Nittler, L. R., Weider, S. Z., Starr, R. D., Chabot, N., Denevi, B. W., Ernst, C. M., et al. (2014). Sulfur-Depleted Composition of Mercury's Largest Pyroclastic Deposit: Implications for Explosive Volcanism and Surface Reflectance on the Innermost Planet. *Lunar and Planetary Science Conference*, *45*, 1391.

Nittler, Larry R., Starr, R. D., Weider, S. Z., McCoy, T. J., Boynton, W. V., Ebel, D. S., et al. (2011). The major-element composition of Mercury's surface from MESSENGER X-ray spectrometry. *Science*, *333*(6051), 1847–1850. https://doi.org/10.1126/science.1211567

Nittler, Larry R, Chabot, N. L., Grove, T. L., & Peplowski, P. N. (2018). The Chemical Composition of Mercury. In S. C. Solomon, L. R. Nittler, & B. J. Anderson (Eds.), *Mercury, The View After MESSENGER* (1st ed., pp. 30–51). Cambridge University Press.

O'Neill, H. S. C., & Mavrogenes, J. A. (2002). The Sulfide Capacity and the Sulfur Content at Sulfide Saturation of Silicate Melts at 1400°C and 1 bar. *Journal of Petrology*, *43*(6), 1049–1087. https://doi.org/10.1093/petrology/43.6.1049

Renggli, King, P. L., Henley, R. W., Guagliardo, P., McMorrow, L., Middleton, J. P., & Turner, M. (2019). An experimental study of SO2 reactions with silicate glasses and supercooled melts in the system anorthite–diopside–albite at high temperature. *Contributions to Mineralogy and Petrology*, *174*(1), 3. https://doi.org/10.1007/s00410-018-1538-2

562 Renggli, Palm, A. B., King, P. L., & Guagliardo, P. (2019). Implications of Reactions Between SO2
563 and Basaltic Glasses for the Mineralogy of Planetary Crusts. *Journal of Geophysical Research:*
564 *Planets*, *124*(10), 2563–2582. https://doi.org/10.1029/2019JE006045
565 Renggli, C. J., & Klemme, S. (2020). Experimental constraints on metal transport in fumarolic gases.
566 *Journal of Volcanology and Geothermal Research*, *400*, 106929.
567 https://doi.org/10.1016/j.jvolgeores.2020.106929
568 Renggli, C. J., & Klemme, S. (2021). Experimental Investigation of Apollo 16 "Rusty Rock" Alteration
569 by a Lunar Fumarolic Gas. *Journal of Geophysical Research: Planets*, *126*(2), e2020JE006609.
570 https://doi.org/10.1029/2020JE006609
571 Renggli, Christian J, & King, P. L. (2018). SO2 Gas Reactions with Silicate Glasses. *Reviews in*
572 *Mineralogy and Geochemistry*, *84*, 229–255.
573 Renggli, C.J., Klemme, S., Morlok, A., Berndt, J., Weber, I., Hiesinger, H., & King, P. L. (2022).
574 Sulfides and hollows formed on Mercury's surface by reactions with reducing S-rich gases.
575 *Earth and Planetary Science Letters*, *593*, 117647. https://doi.org/10.1016/j.epsl.2022.117647
576 Tappert, M. C., Rivard, B., Tappert, R., & Feng, J. (2013). Using reflectance spectroscopy to estimate
577 the orientation of quartz crystals in rocks. *The Canadian Mineralogist*, *51*(3), 405–413.
578 https://doi.org/10.3749/canmin.51.3.405
579 Vander Kaaden, K. E., M. McCubbin, F., R. Nittler, L., N. Peplowski, P., Z. Weider, S., A. Frank, E.,
580 & J. McCoy, T. (2017). Geochemistry, mineralogy, and petrology of boninitic and komatiitic
581 rocks on the mercurian surface: Insights into the mercurian mantle. *Icarus*, *285*, 155–168.
582 https://doi.org/10.1016/j.icarus.2016.11.041
583 Varatharajan, I., Maturilli, A., Helbert, J., Alemanno, G., & Hiesinger, H. (2019). Spectral behavior of
584 sulfides in simulated daytime surface conditions of Mercury: Supporting past (MESSENGER)
585 and future missions (BepiColombo). *Earth and Planetary Science Letters*, *520*, 127–140.
586 https://doi.org/10.1016/j.epsl.2019.05.020
587 Weber, I., Stojic, A. N., Morlok, A., Reitze, M. P., Markus, K., Hiesinger, H., et al. (2020). Space
588 weathering by simulated micrometeorite bombardment on natural olivine and pyroxene: A

589 coordinated IR and TEM study. *Earth and Planetary Science Letters*, *530*, 115884.
590 https://doi.org/10.1016/j.epsl.2019.115884
591 Weider, S. Z., Nittler, L. R., Starr, R. D., McCoy, T. J., Stockstill-Cahill, K. R., Byrne, P. K., et al.
592 (2012). Chemical heterogeneity on Mercury's surface revealed by the MESSENGER X-Ray
593 Spectrometer: CHEMICAL HETEROGENEITY ON MERCURY. *Journal of Geophysical*
594 *Research: Planets*, *117*(E12), n/a-n/a. https://doi.org/10.1029/2012JE004153
595 Weider, S. Z., Nittler, L. R., Starr, R. D., Crapster-Pregont, E. J., Peplowski, P. N., Denevi, B. W., et
596 al. (2015). Evidence for geochemical terranes on Mercury: Global mapping of major elements
597 with MESSENGER's X-Ray Spectrometer. *Earth and Planetary Science Letters*, *416*, 109–
598 120. https://doi.org/10.1016/j.epsl.2015.01.023
599 Weider, S. Z., Nittler, L. R., Murchie, S. L., Peplowski, P. N., McCoy, T. J., Kerber, L., et al. (2016).
600 Evidence from MESSENGER for sulfur- and carbon-driven explosive volcanism on Mercury.
601 *Geophysical Research Letters*, *43*(8), 2016GL068325. https://doi.org/10.1002/2016GL068325
602 Zolotov, Mikhail Y., Sprague, A. L., Hauck, S. A., Nittler, L. R., Solomon, S. C., & Weider, S. Z.
603 (2013). The redox state, FeO content, and origin of sulfur-rich magmas on Mercury. *Journal of*
604 *Geophysical Research: Planets*, *118*(1), 138–146. http://dx.doi.org/10.1029/2012JE004274
605 Zolotov, Mikhail Yu. (2011). On the chemistry of mantle and magmatic volatiles on Mercury. *Icarus*,
606 *212*(1), 24–41. https://doi.org/10.1016/j.icarus.2010.12.014
607
608

Figure 1.

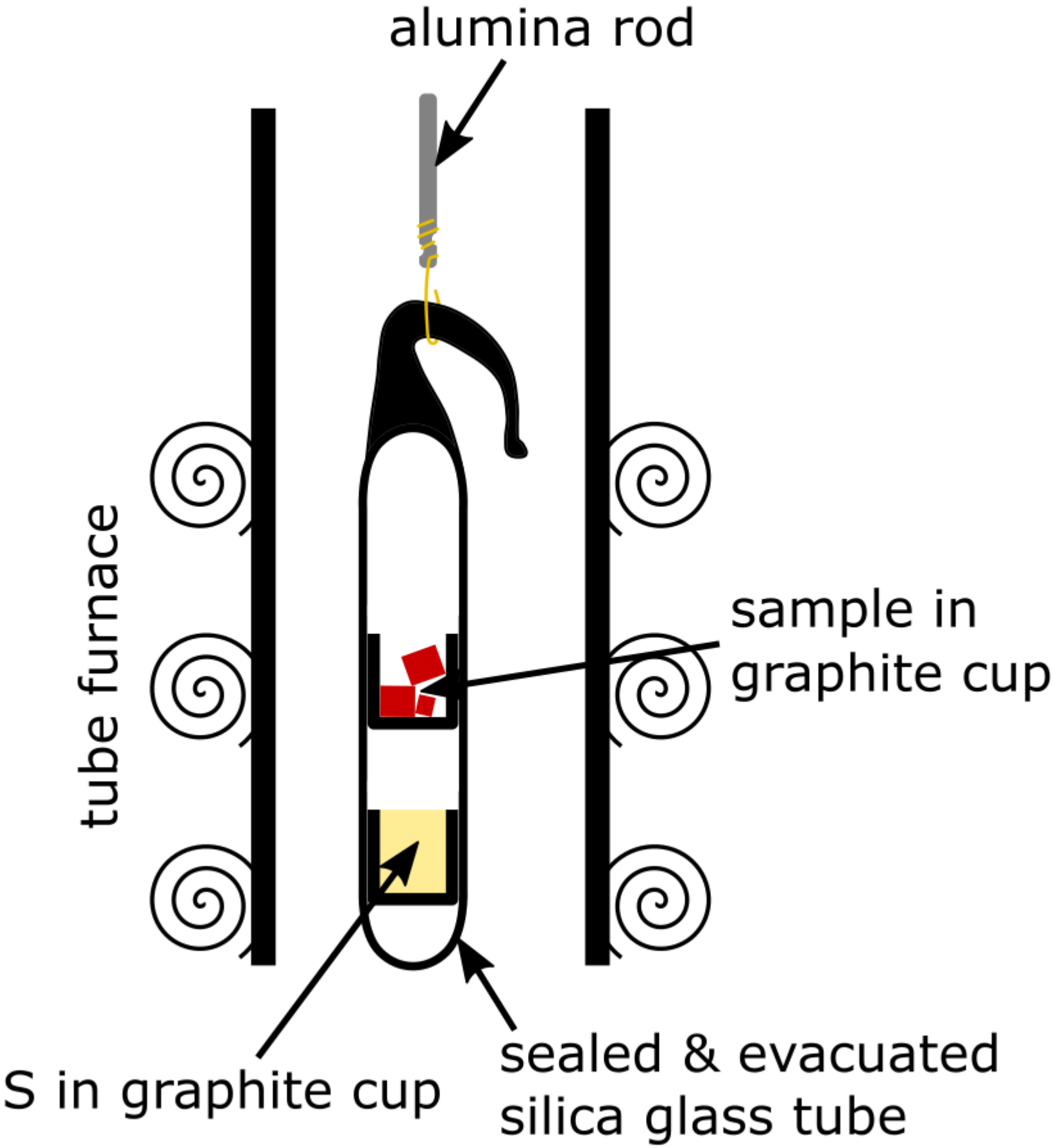
alumina rod
tube furnace
sample in
graphite cup
S in graphite cup
sealed & evacuated
silica glass tube

Figure 2.

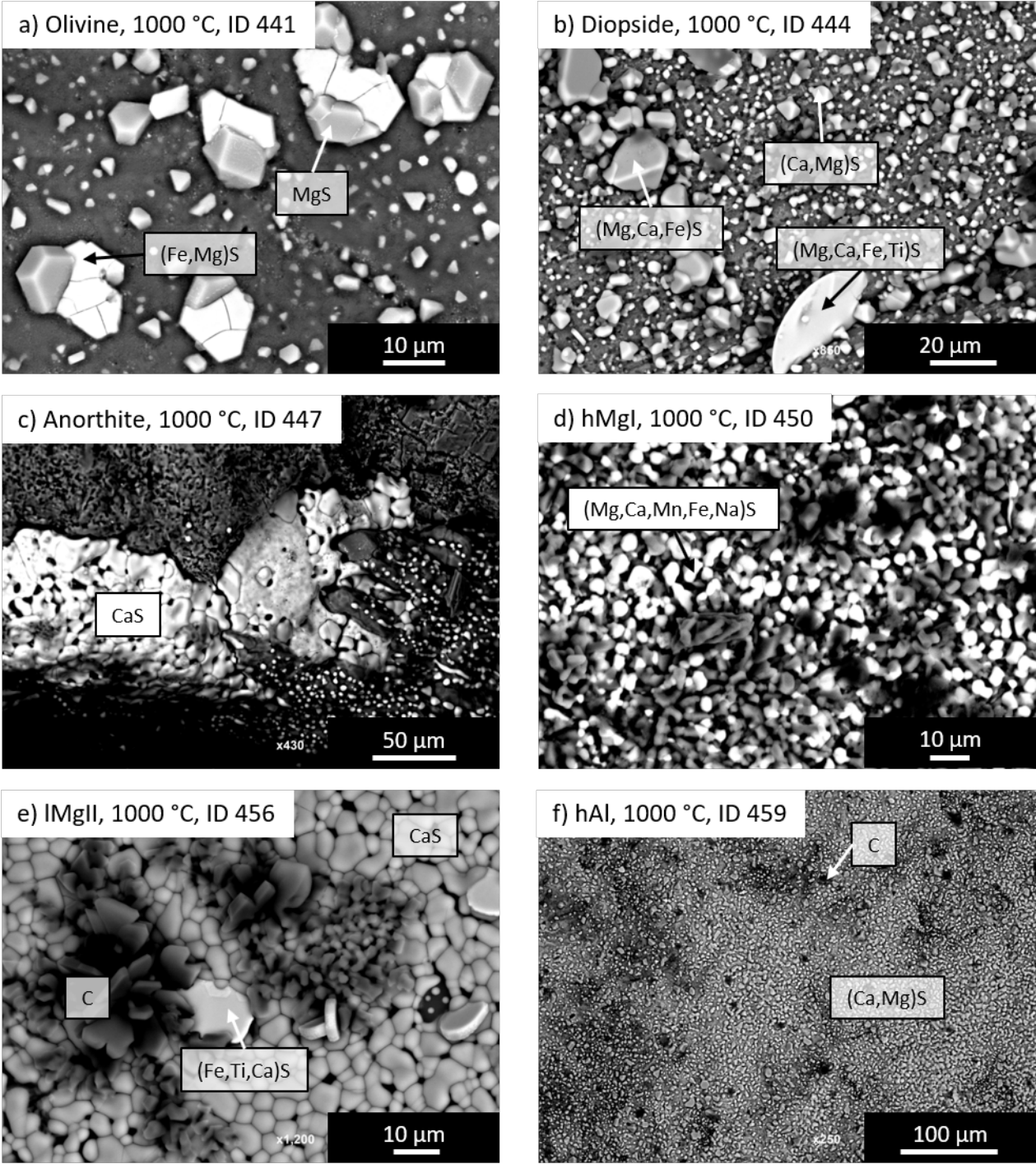
a) Olivine, 1000 °C, ID 441
MgS
(Fe,Mg)S
10 µm
b) Diopside, 1000 °C, ID 444
(Ca,Mg)S
(Mg,Ca,Fe)S
(Mg,Ca,Fe,Ti)S
20 µm
c) Anorthite, 1000 °C, ID 447
CaS
x430
50 µm
d) hMgI, 1000 °C, ID 450
(Mg,Ca,Mn,Fe,Na)S
10 µm
e) lMgII, 1000 °C, ID 456
CaS
C
(Fe,Ti,Ca)S
x1,200
10 µm
f) hAl, 1000 °C, ID 459
C
(Ca,Mg)S
x250
100 µm

Figure 3.

a) Olivine

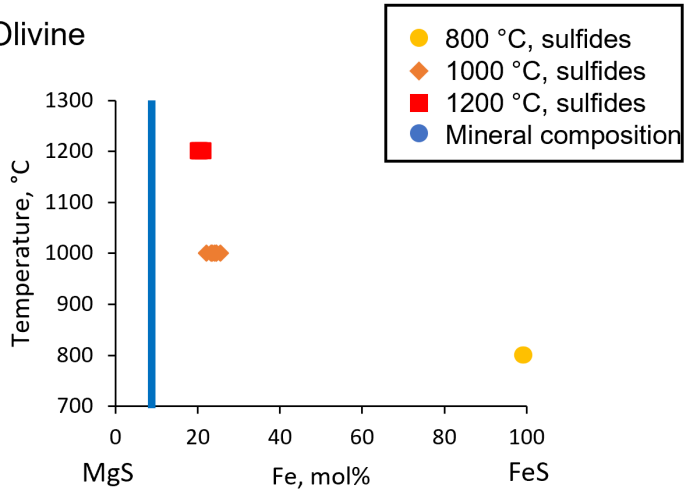

b) Diopside

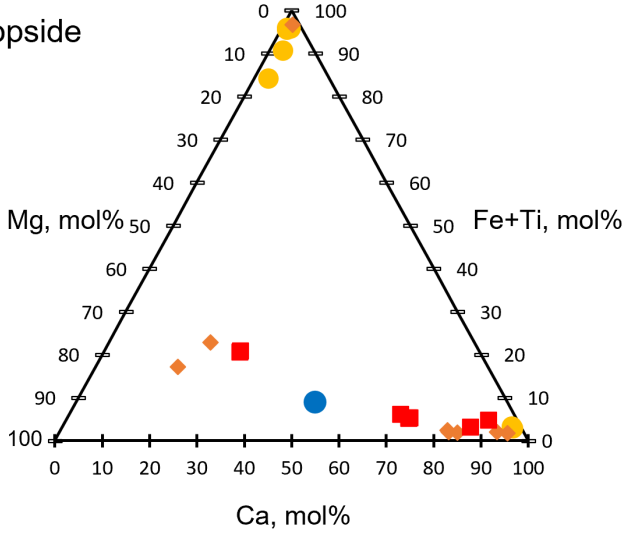

Figure 4.

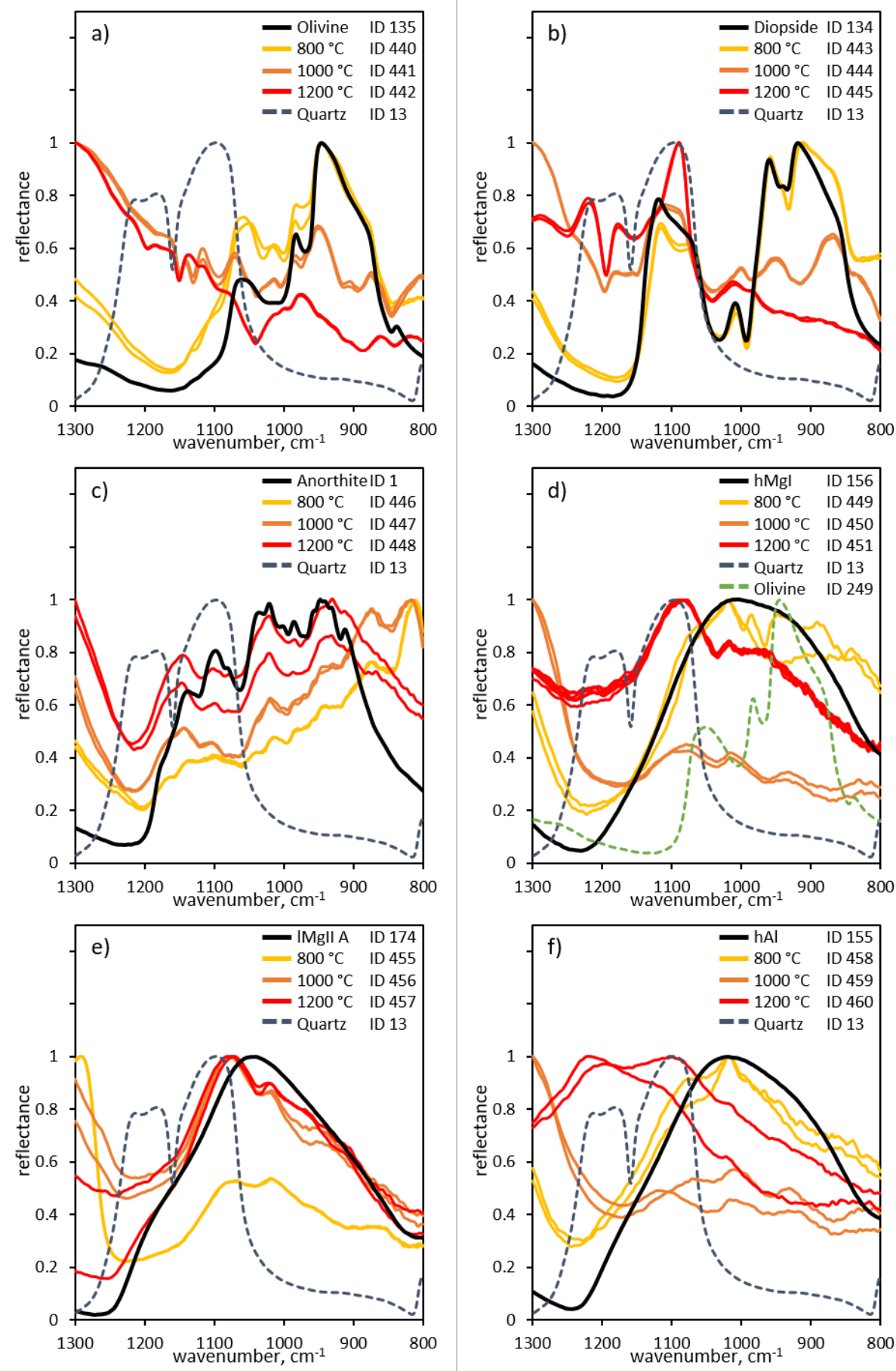
a)
Olivine ID 135
800 °C ID 440
1000 °C ID 441
1200 °C ID 442
Quartz ID 13
b)
Diopside ID 134
800 °C ID 443
1000 °C ID 444
1200 °C ID 445
Quartz ID 13
c)
Anorthite ID 1
800 °C ID 446
1000 °C ID 447
1200 °C ID 448
Quartz ID 13
d)
hMgI ID 156
800 °C ID 449
1000 °C ID 450
1200 °C ID 451
Quartz ID 13
Olivine ID 249
e)
lMgII A ID 174
800 °C ID 455
1000 °C ID 456
1200 °C ID 457
Quartz ID 13
f)
hAl ID 155
800 °C ID 458
1000 °C ID 459
1200 °C ID 460
Quartz ID 13
reflectance
wavenumber, cm-1
1300
1200
1100
1000
900
800
0
0.2
0.4
0.6
0.8
1

Figure 5.

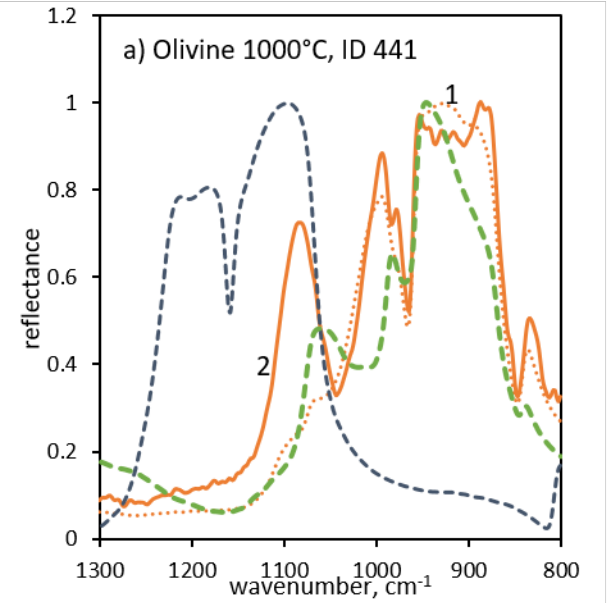

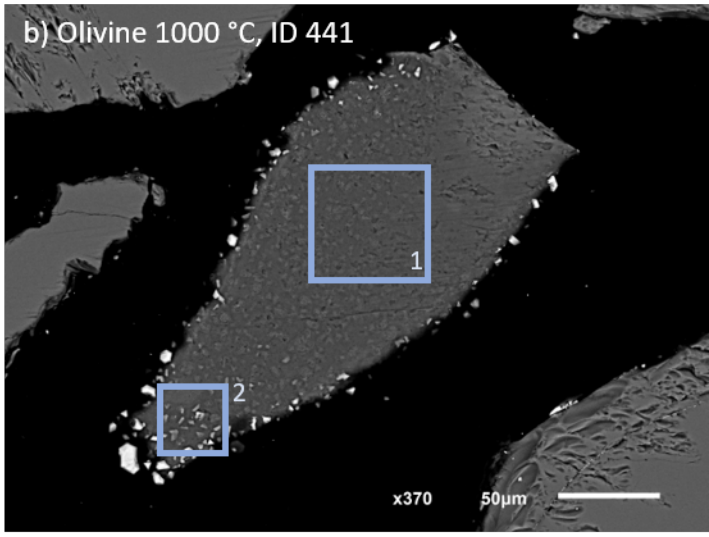

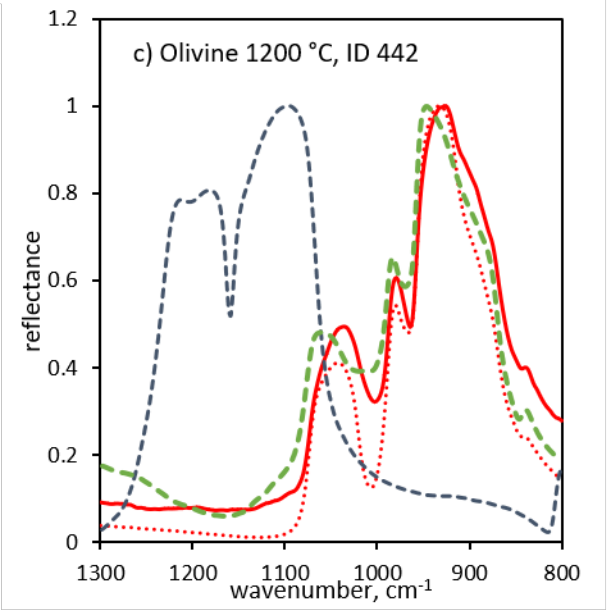

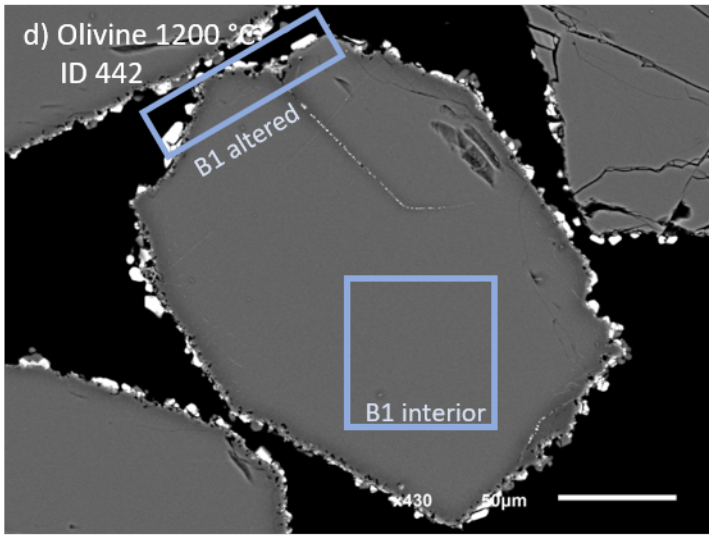

800 °C
1200 °C
Olivine ID 135
Quartz ID 13
interior of sample, no/less alteration
altered surface or near-surface

Figure 6.

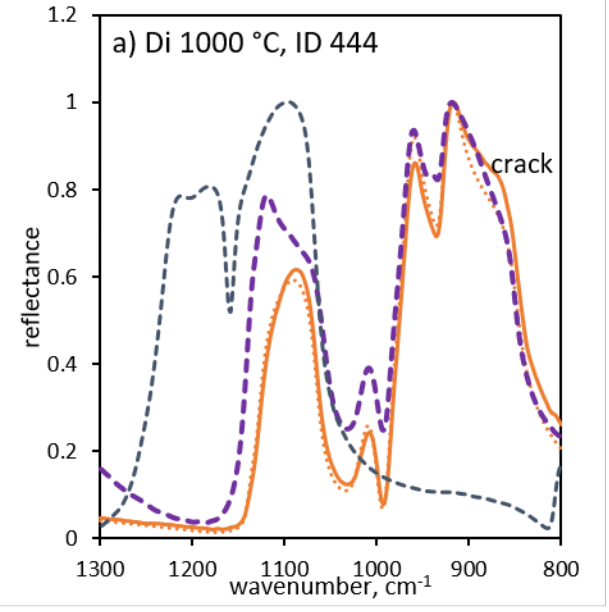

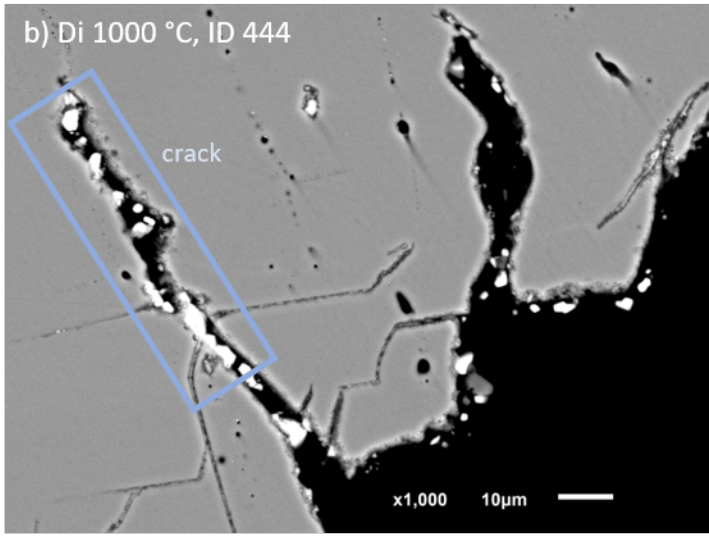

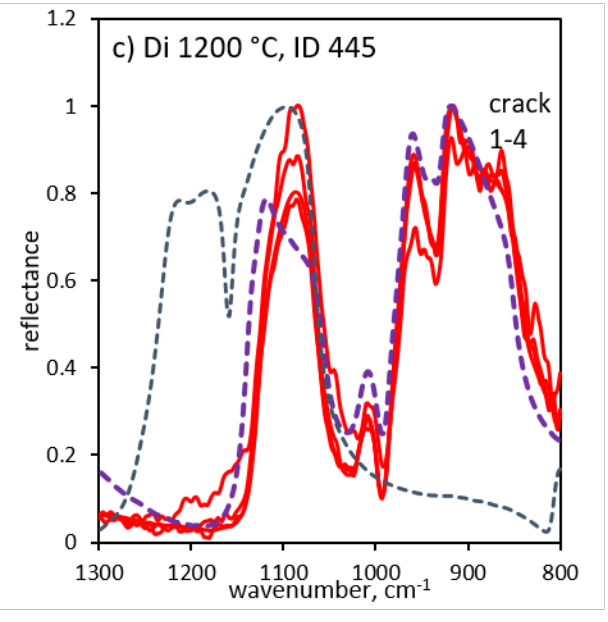

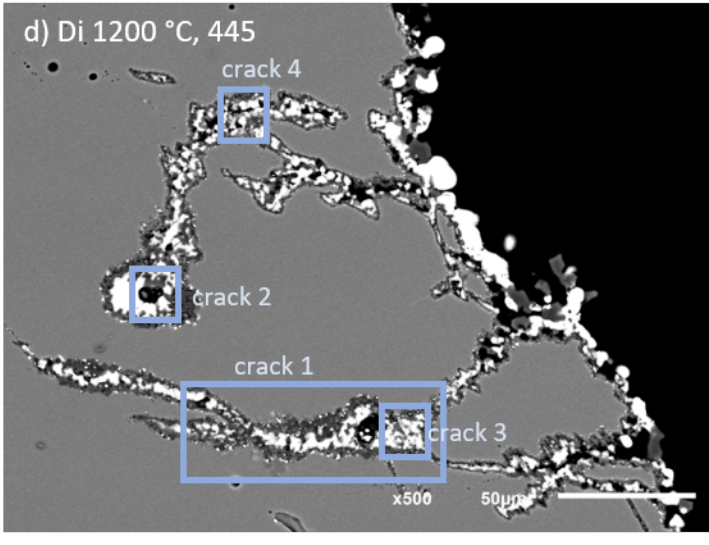

1000 °C
1200 °C
Diopside ID 134
Quartz ID 13
interior of sample, no/less alteration
altered surface or near-surface

Figure 7.

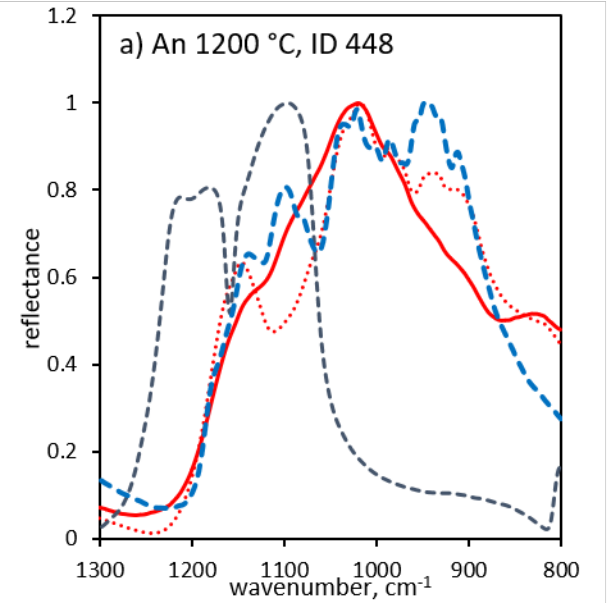

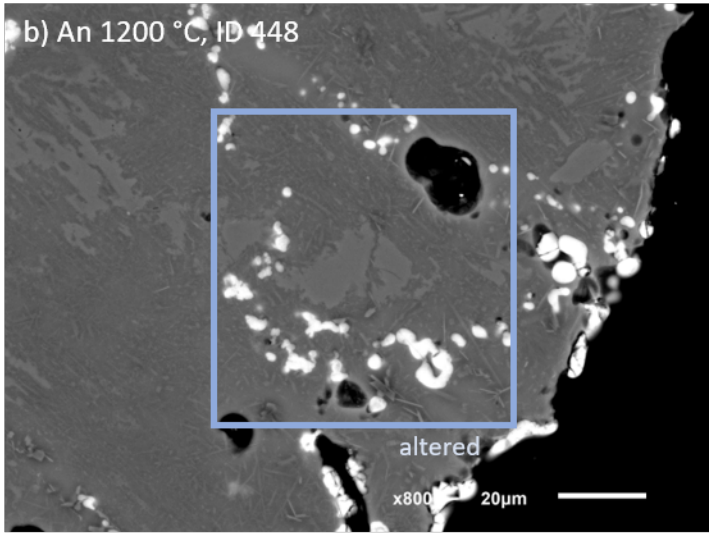

1200 °C

Anorthite ID 1

Quartz ID 13

interior of sample, no/less alteration

altered surface or near-surface

Figure 8.

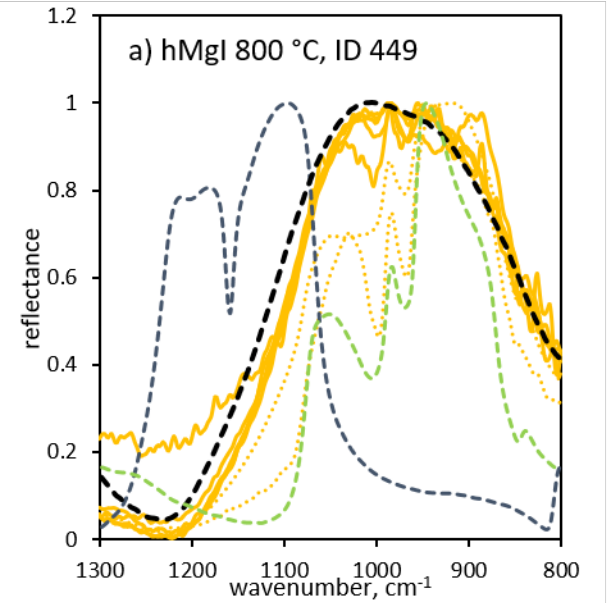

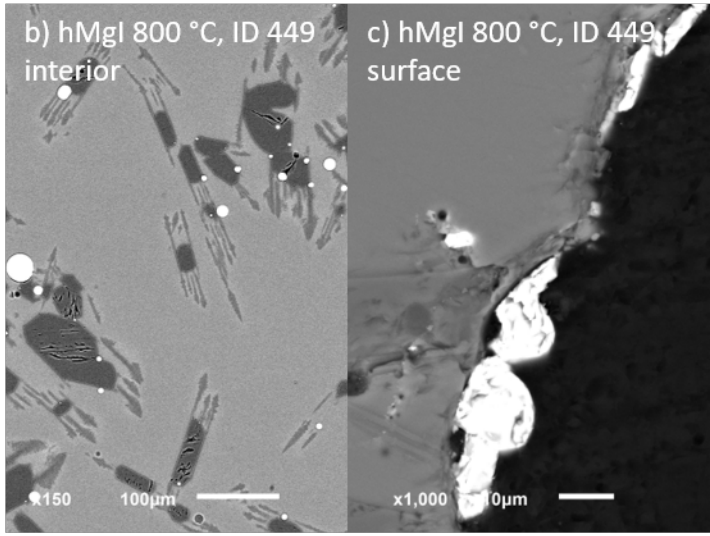

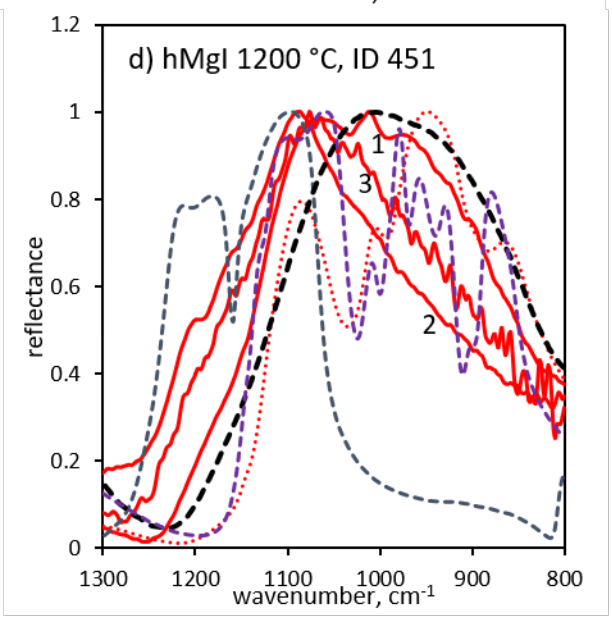

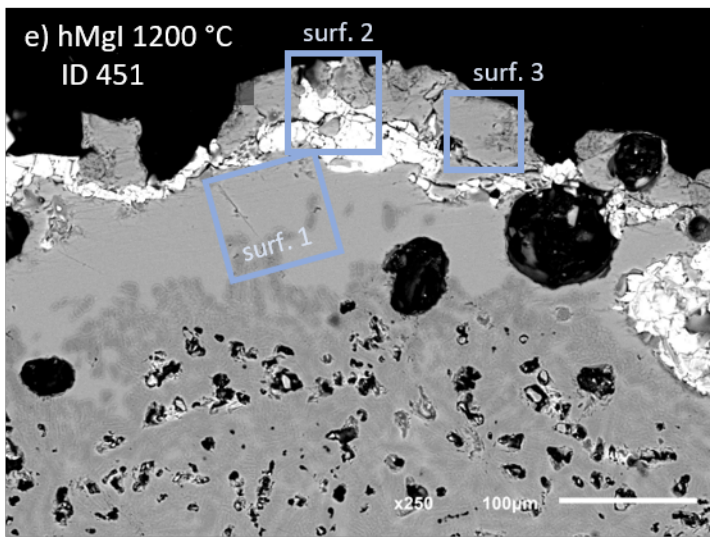

800 °C
1200 °C
hMgI ID 156
Quartz ID 13
Olivine ID 249
Enstatite ID 53
interior of sample, no/less alteration
altered surface or near-surface

Figure 9.

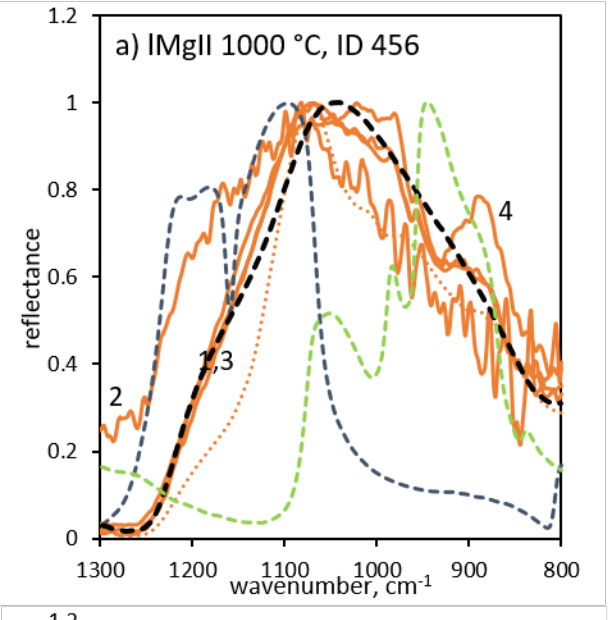

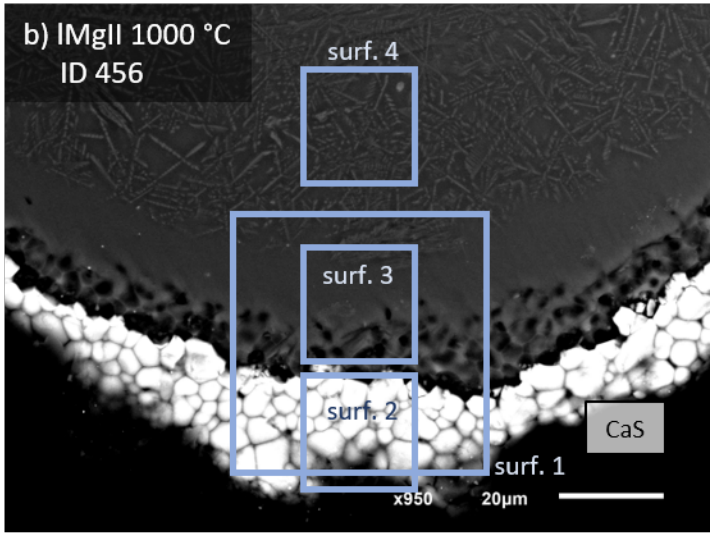

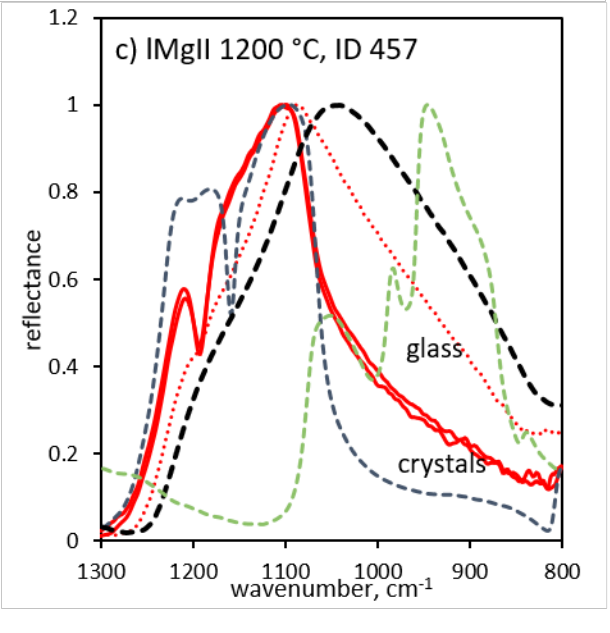

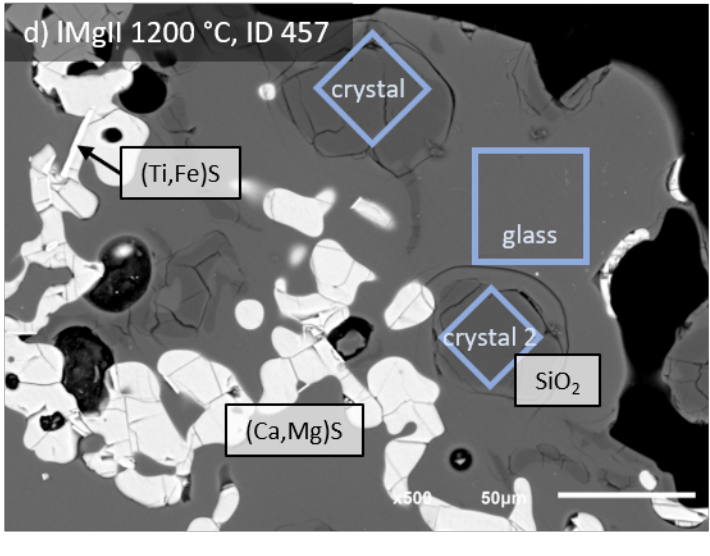

1000 °C
1200 °C
lMgII A 174
Quartz 13
Olivine 249
interior of sample, no/less alteration
altered surface or near-surface

Figure 10.

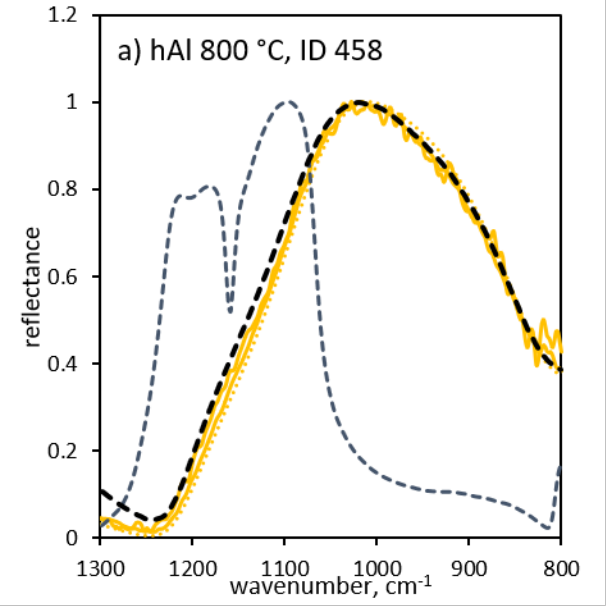

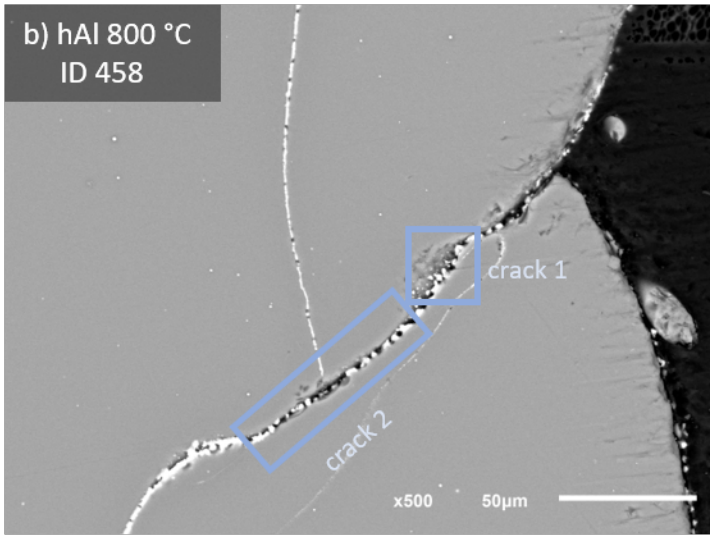

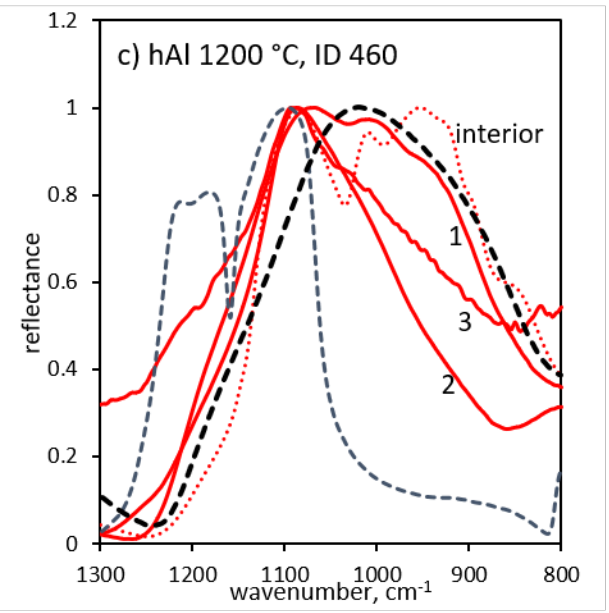

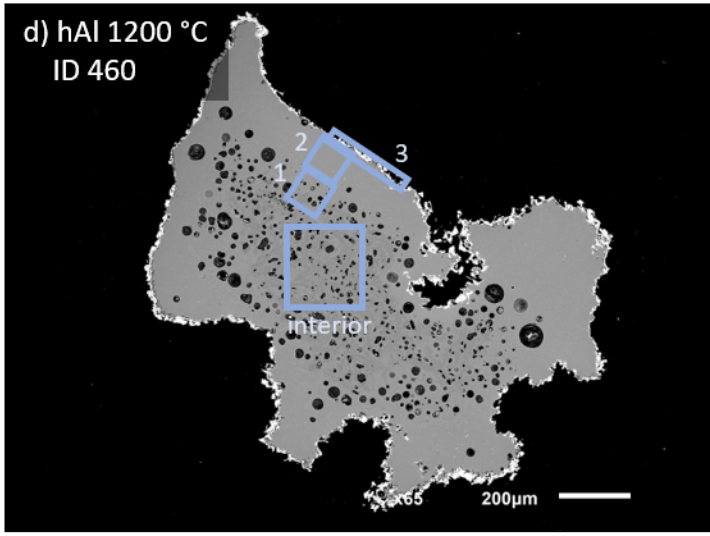

800 °C
1200 °C
hAl ID 155
Quartz ID 13
interior of sample, no/less alteration
altered surface or near-surface